Draft version December 7, 2011
Preprint typeset using LaTeX style emulateapj v. 11/10/09

THE GALEX ARECIBO SDSS SURVEY V: THE RELATION BETWEEN THE HI CONTENT OF GALAXIES AND METAL ENRICHMENT AT THEIR OUTSKIRTS

Sean M. Moran[1], Timothy M. Heckman[1], Guinevere Kauffmann[2], Romeel Davé[3] Barbara Catinella[2], Jarle Brinchmann[4], Jing Wang[2], David Schiminovich[5], Amélie Saintonge[6], Javier Gracia-Carpio[6], Linda Tacconi[6], Riccardo Giovanelli[7], Martha Haynes[7], Silvia Fabello[2], Cameron Hummels[5], Jenna Lemonias[5], & Ronin Wu[8]

Draft version December 7, 2011

ABSTRACT

We have obtained long-slit spectra of 174 star-forming galaxies with stellar masses greater than $10^{10} M_\odot$ from the *GALEX* Arecibo SDSS (GASS) survey. These galaxies have both HI and H_2 mass measurements. The average metallicity profile is strikingly flat out to R_{90}, the radius enclosing 90% of the *r*-band light. Metallicity profiles which decline steadily with radius are found primarily for galaxies in our sample with low stellar mass ($\text{Log}(M_*) < 10.2$), concentration, and/or mean stellar mass density. Beyond $\sim R_{90}$, however, around 10 percent of the galaxies in our sample exhibit a sharp downturn in metallicity. Remarkably, we find that the magnitude of the outer metallicity drop is well correlated with the *total* HI content of the galaxy (measured as $f_{HI} = M_{HI}/M_*$). We examine the radial profiles of stellar population ages and star formation rate densities, and conclude that the galaxies with largest outer metallicity drops are actively growing their stellar disks, with mass doubling times across the whole disk only one third as long as a typical GASS galaxy. We also describe a correlation between *local* stellar mass density and metallicity, which is valid across all galaxies in our sample. We argue that much of the recent stellar mass growth at the edges of these galaxies can be linked to the accretion or radial transport of relatively pristine gas from beyond the galaxies' stellar disks.

Subject headings: galaxies: star formation – galaxies: evolution – galaxies: ISM – galaxies: stellar content

1. INTRODUCTION

A proper characterization of the ages and metallicities of the stars in spiral galaxies, as well as the radial dependence of the metallicity of stars and gas in these systems, has long been recognized as a key stepping-stone to unravelling disk galaxy formation processes, including the roles of gas accretion, supernovae-driven outflows and the radial migration of stars (Quirk & Tinsley 1973; Tinsley 1980; Lacey & Fall 1985; Wyse & Silk 1989; Kauffmann 1996; Chiappini et al. 1997; Schönrich & Binney 2009).

There have, however, been rather few systematic studies of how radial star formation and metal abundance gradients vary across *populations* of disk galaxies. Vila-Costas & Edmunds (1992) carried out an analysis of abundance gradients in a sample of 30 spiral galaxies with spectroscopy from the literature. Barred galaxies were found to have flatter abundance gradients than un-barred galaxies. When the analysis was restricted to un-barred galaxies, gradients were found to be stronger in late-type galaxies (see also (see also Oey & Kennicutt 1993). Vila-Costas & Edmunds also found the the central metallicities of spiral galaxies were correlated with both the total stellar mass of the galaxy, and the local central surface density of stars. Zaritsky, Kennicutt & Huchra (1994) obtained uniform HII-region based abundance gradients for a sample of 39 nearby disk galaxies. In this study, the slopes of radial abundance gradients, when expressed in units of dex/isophotal radius, did not exhibit any significant correlation with luminosity or Hubble type, but it was later noted by Garnett et al. (1997) that gradients expressed in dex/kpc steepen with decreasing luminosity. Further observations by van Zee et al. (1998) focused on increasing the number of measurements in the outer regions of galaxies; they identified several galaxies where the fitted gradient changed significantly with the addition of higher-radius data. Recently, Moustakas et al. (2010) presented resolved metallicity measurements for a sample of nearby galaxies from the *Spitzer* Nearby Galaxies Survey (SINGS, Kennicutt et al. 2003a), and pointed out that derived metallicity gradients can be sensitive to the methodology used to calibrate the strong-line abundance estimates.

A complete, systematic and carefully-executed survey of metallicity gradients in a large sample of nearby disk galaxies is urgently needed to help put into context some recent studies that have reported unexpected or peculiar metallicity profiles in a number of individual galaxies. A number of these (e.g., Werk et al. 2011; Rupke et al. 2010; Kewley et al. 2010; Bresolin et al. 2009) find surprisingly flat metallicity gradients, even out to extreme

---

moran@pha.jhu.edu
[1] Department of Physics and Astronomy, The Johns Hopkins University, 3400 N. Charles Street, Baltimore, MD 21218, USA
[2] Max Planck Institut für Astrophysik, Karl-Schwarzschild-Str. 1, D-85741 Garching, Germany
[3] Astronomy Department, University of Arizona, Tucson, AZ 85721, USA
[4] Leiden Observatory, Leiden University, 2300 RA, Leiden, The Netherlands
[5] Department of Astronomy, Columbia University, 550 West 120th Street, New York, New York 10027, USA
[6] Max Planck Institut für Extraterrestrische Physik, Giessesbach-Str., 85748 Garching, Germany
[7] Department of Astronomy, 610 Space Sciences Building, Cornell University, Ithaca,NY 14853, USA
[8] Commissariat à l'Energie Atomique (CEA), 91191 Gif-sur-Yvette, France

distances, both for interacting galaxies and peculiarly gas-rich objects, in contrast with earlier work documenting low metallicities or large drops in the extreme outskirts of galaxies (e.g., Ferguson et al. 1998; Kennicutt et al. 2003b). The more recent papers argue that these differences reflect the important role of gas inflows and outflows, as well as mixing, in determining how metallicity changes as a function of radius in galaxies.

In order to learn more about the relations between cold gas and star formation in nearby galaxies, we are carrying out the *GALEX* Arecibo SDSS Survey (GASS)[9] (Catinella et al. 2010, hereafter C10). GASS is designed to measure the neutral hydrogen content of a representative sample of $\sim$ 1000 galaxies uniformly selected from the Sloan Digital Sky Survey (SDSS, York et al. 2000) and *Galaxy Evolution Explorer* (*GALEX*, Martin et al. 2005) imaging survey, with stellar masses in the range $10^{10} - 10^{11.5}$M$_\odot$ and redshifts in the range $0.025 < z < 0.05$. GASS observations are designed to detect HI down to a gas-fraction limit of 1.5-5%, so the full GASS sample will be the first HI survey able to place meaningful, unbiased constraints on the atomic gas reservoirs that may contribute to future growth in massive galaxies. We are also pursuing a companion project on the IRAM 30m telescope, COLD GASS[10], which has obtained accurate and homogeneous molecular gas masses for a subset of 350 galaxies from the GASS sample (Saintonge et al. 2011). These data will allow us to characterize the balance between atomic and molecular gas in the galaxies in our sample, and understand the physical processes that determine how the condensed baryons are partitioned into stars, HI and H$_2$ in the local Universe.

The third component of the GASS survey, and the subject of the current paper, is a follow-up campaign to obtain long-slit spectroscopy for the COLD GASS subset of 350 galaxies. Such spectra allow us to link the measured gas contents of galaxies to their rotational dynamics, metal abundance gradients and resolved star formation histories. In this first paper in our series on the GASS long-slit data, we focus on studying the gas-phase metallicities of star-forming regions as a function of radius for a partially-complete sample of 174 GASS galaxies.

In §2 & 3 below, we will describe our observations, data reduction pipeline, and our methodology for measurement of metallicities. In §4, we will show how metallicity gradients vary as a function of both global and localized galaxy properties. In §5, we will present a remarkably tight relation between the total HI content and metallicity in the outer regions of galactic disks, and examine in detail a subset of galaxies exhibiting steep metallicity drops in their outer disks. In the following, we adopt a standard ΛCDM cosmology with $\mathrm{H}_0 = 70\mathrm{km\,s}^{-1}\,\mathrm{Mpc}^{-1}$, $\Omega_m = 0.3$ and $\Omega_\Lambda = 0.7$. Stellar masses and star formation rates are calculated assuming a Kroupa (2001) initial mass function (IMF).

2. OBSERVATIONS

GASS observations of the 21cm line of neutral hydrogen have been obtained with the L-band Wide receiver of the Arecibo telescope. Integration times are set such that we detect any HI down to a limiting HI fraction ($f_{HI} = M_{HI}/M_*$) of 3.5% or less. Details of the HI sample, observations, and mass calculations are given in C10.

Likewise, molecular gas masses are determined through observations of the CO ($J = 1 - 0$) line using the IRAM 30m telescope, to similar mass fraction limits, as part of the COLD GASS program. Details of the observations and mass determinations are provided in Saintonge et al. (2011).

We note that both HI and CO observations provide only *integrated* measures of total atomic or molecular gas mass, respectively. Thus, when comparing to the results from our *resolved* spectroscopy, it is important to keep in mind that our current data gives no insight into the spatial distribution of the gas.

Long-slit spectroscopy of 174 galaxies in the GASS and COLD GASS samples was obtained over the period 2008 October to 2010 November, using both the Blue Channel Spectrograph on the 6.5m MMT telescope on Mt. Hopkins, AZ, and the Dual Imaging Spectrograph (DIS) on the Apache Point 3.5m. We observe each galaxy with the slit aligned along the major axis of the galaxy, with a slit length that is much larger than the size of the galaxy. Our sample contains 131 galaxies with MMT spectra, and 43 with APO spectra.

All MMT observations were obtained through a $1.25''$wide slit covering the spectral range $\sim 3900-7000$Å at a spectral resolution of $\sim$ 4Å FWHM, equivalent to $\sigma \sim 90\mathrm{km\ s}^{-1}$ in the rest frame of a typical galaxy. In the spatial direction, pixels are $0.3''$wide, and we typically obtained 2x900s exposures for each galaxy.

APO observations were taken through a slightly wider, $1.5''$slit, with spatial sampling of $0.4''$. Typical exposure times were somewhat longer (2x1200s). The wavelength range of APO spectra is more extended than MMT, covering from $\sim 3800 - 9000$Å at a spectral resolution of 6–8 Å or $\sim 150\mathrm{km\ s}^{-1}$.

Data were reduced in IDL with routines from the publicly available Low-Redux package[11] maintained by X. Prochaska, which itself is an adaptation of the Princeton SDSS reduction code[12] to more general long-slit reductions. The code performs standard biasing, flat-fielding, cosmic-ray rejection, and sky estimation on each exposure. We then co-add the sky-subtracted exposures through a custom-written routine that verifies and adjusts the alignment of exposures before co-addition. Flux calibration was achieved via observation of spectrophotometric standards BD+17 4708, BD+33 2642, or Feige 67.

APO spectra are recorded as separate files for the blue and the red channels; these are reduced independently, as described above, and then joined. To eliminate any inconsistency in the flux scaling between the two channels, we rescale the spectra as follows: we select a 75Å window near 5450Å where the dichroic element that splits the incoming flux has non-zero transmission into both channels. Within this window, we measure the flux normalization of each spectrum, calculate the average of the two, and place both on a uniform flux scale by apply-

---

[9] http://www.mpa-garching.mpg.de/GASS

[10] http://www.mpa-garching.mpg.de/COLD_GASS

[11] http://www.ucolick.org/~xavier/LowRedux/

[12] http://spectro.princeton.edu

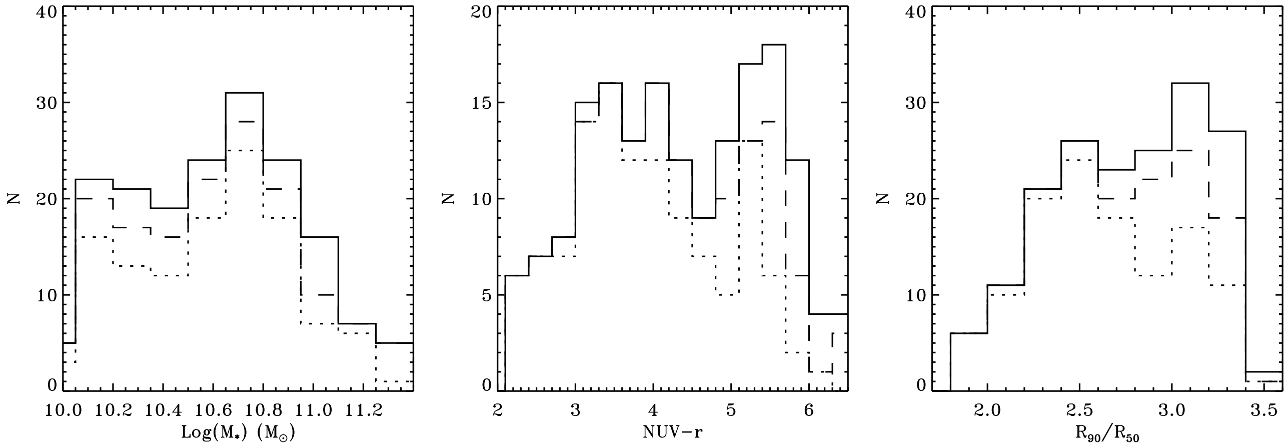

Figure 1. Histograms showing the distribution of stellar mass, NUV$-r$ colour (observed frame), and concentration index R_{90}/R_{50} for our full spectroscopic sample (solid), complete star-forming sample (dashed), and sample with extended ($R > 0.7R_{90}$) star formation (dotted).

ing the average scaling to both spectra. The blue and the red spectra can then be joined through a simple concatenation, averaging values within the small window of overlap.

Thanks to existing, very accurately calibrated SDSS photometry and spectra, we are able to refine our flux calibrations (for both MMT and concatenated APO spectra) by matching to SDSS. First, we convolve our spatially integrated spectra with the response functions of the SDSS g and r filters. We next measure g and r magnitudes directly on the SDSS images through an aperture matched to our slit, following the procedure of Wang et al. (2011a), described further in §3. We then apply the average difference in g and r-band magnitudes as a scalar correction factor to our spectrum. Such corrections allow us to accurately flux calibrate spectra that were taken in non-photometric conditions. Typical correction factors are ~ 0.25 mag for observations taken through light cloud cover. Typically the corrections derived from g band alone versus those for r differ by less than 0.02 mag, verifying that our *relative* spectrophotometry is quite accurate. When we compare SDSS fiber spectra to the central portion of our slit spectra, matched as well as possible to the SDSS $3''$aperture, the resulting spectrophotometry agrees with SDSS to better than 10% across the full wavelength range.

3. ANALYSIS

In this paper, we focus on a subset of 151 galaxies (out of the 174 galaxies in the GASS spectroscopic sample) where we have detected significant emission lines ($> 3\sigma$) from star forming regions anywhere within the area probed by our spectroscopic slit. We exclude regions contaminated by AGN emission (see below). The presence of emission lines is necessary for measuring gas-phase metallicities. Within the star-forming subset of 151 galaxies, 119 have star formation that can be traced to at least $2R_{50} \sim 0.7R_{90}$, where R_{50} and R_{90} are the radii enclosing 50% and 90% of the galaxy's r-band light, respectively. In §5, which discusses metallicities in the outer regions of galaxies, the galaxies are drawn from this subsample.

In Figure 1, we show how these various subsamples are distributed in stellar mass, NUV$-r$ color (observed frame), and concentration index (R_{90}/R_{50}). We note first that the 174-galaxy spectroscopic sample has the same distribution of galaxy properties as the full GASS sample of 1000 galaxies. Both are selected to have a flat stellar mass distribution (left histogram in Figure 1). Further restricting the sample to, first, star-forming galaxies, and second, galaxies with star formation at *large radius*, serves only to exclude a number of red, high concentration galaxies. We note that galaxies across the stellar mass range $10 < Log(M_*) < 11$ are still well sampled despite these cuts.

We first follow the procedure outlined in Moran et al. (2010) to determine galaxy rotation curves, which allows us to correct the spectrum from each individual row to a common rest frame before binning. This helps to avoid velocity blurring of the coadded spectrum. (Note that we will not otherwise discuss galaxy rotation curves and dynamics in this paper). For each two-dimensional spectrum sampled at 0.3 or 0.4 arcsecond resolution, we then perform adaptive binning in the spatial direction to ensure an adequate S/N in each spatial bin in our analysis. Beginning at the galaxy center, defined as the spatial row with peak flux, we coadd bins working outward one row at a time, stopping when we reach an integrated S/N of 15 (per Angstrom). If S/N does not reach 15 by the time $3''$of slit has been coadded, then we stop at that width so long as S/N is greater than 10, and begin a new bin. We proceed outwards in this manner, with three additional breakpoints where the S/N requirements are changed: we require $S/N > 10$ up to size $4.5''$, followed by $S/N > 8$ up to size $6''$, and $S/N > 6$ at distances beyond that. The procedure terminates when further binning fails to add to either the continuum S/N or the S/N in the Hα line, which is tracked to ensure that we do not discard any faint emission. We note, also, that all bins are constrained to be at least as long as the slit width ($1.25''$or $1.5''$), since finer binning does not provide added spatial information.

The end result of this process is a set of spectra for each galaxy where bin size generally increases with radius, but the S/N in each bin falls much more slowly with radius than it would if we had used uniform bin sizes.

We employ a modified version of the technique of Tremonti et al. (2004, hereafter T04) to measure the

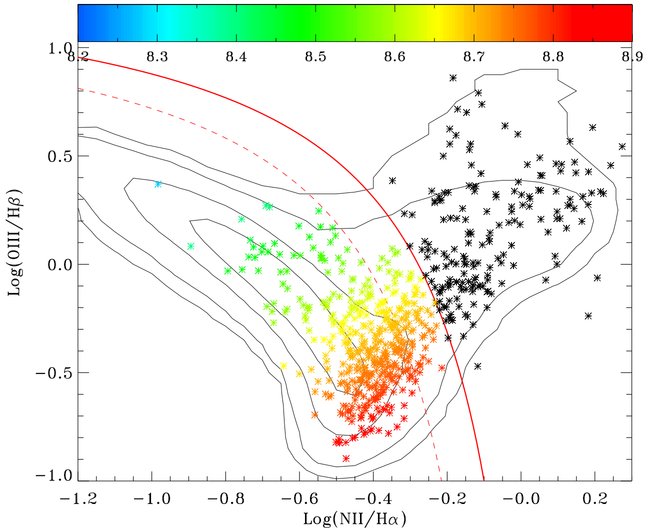

Figure 2. Line ratio diagram for all independent spatial bins with significant ($> 5\sigma$) emission in all four lines, drawn from all 174 spectra in our sample. Colored points indicate galaxy regions of varying metallicities, as indicated in the color bar at top of the figure. Emission-line regions with line ratios consistent with excitation dominated by an AGN are plotted as black points, and lie above the solid red line. Between the solid and dotted red lines, points may reflect a small AGN contribution to the flux. Contours show where 33%, 67%, 95% and 99% of SDSS galaxies with redshifts in the GASS range ($0.025 < z < 0.05$) lie. Note that for the SDSS galaxies, line ratios are measured within the fiber.

strengths of key emission and absorption lines in each spatial bin for each galaxy, as described in detail in Brinchmann et al. (2004) and Moran et al. (2010). In brief, we fit each spectrum to a linear combination of templates drawn from Bruzual & Charlot (2003) single stellar population models of varying metallicities. Next, we subtract the best-fitting stellar continuum model from the measured spectrum, creating an emission-line only spectrum where the Balmer emission lines can be measured free of contamination from the underlying stellar absorption.

For most spatial bins, our code fits for the best-match velocity dispersion of the continuum spectrum, but for bins with marginal S/N in the continuum ($3 < S/N < 8$ per Angstrom), we instead adopt the median velocity dispersion of all the high S/N bins from the same galaxy.

In cases where only nebular emission is detected, common at the outskirts of some galaxies, no continuum fitting is possible, so we instead fit a low-order polynomial to the spectrum to correct for small imperfections in our sky subtraction, which arise when co-adding across a large portion of the slit. We then measure emission lines using the polynomial-subtracted spectrum.

We fit a Gaussian function to the emission lines, with the width of the Gaussian constrained to a single value for all lines in a given spectrum. As the binned spectra have already had any galactic rotation component removed before coaddition, the choice of a single width for all lines is a reasonable first approximation. The positions of the line centroids are constrained to their rest-wavelengths. In addition to the Balmer lines Hα, Hβ, and Hγ, used to estimate dust extinction and star formation rate (see below), we also measure the forbidden lines [O II] λ5007, [N II] $\lambda\lambda$6548,6584, and, when possible, [O II] $\lambda\lambda$3726,3729 and [S II] $\lambda\lambda$6717,6731, which are required to measure metallicity across each galaxy.

We estimate the dust extinction within the nebular gas by calculating the Balmer decrement, which we define as the ratio of Hα/Hβ to the case B recombination ratio of 2.87 (Osterbrock 1989). We use the formula $E(B-V)_{gas} = 1.97\log(\mathrm{H}\alpha/\mathrm{H}\beta/2.87)$, where we adopt the Calzetti et al. (2000) attenuation curve with $R'_V = 4.05$. We note that all SFRs reported below have been calculated after correcting fluxes for extinction using the Balmer decrement.

After correcting Hα luminosities for dust, we measure star formation rates using the equation in Meurer et al. (2009): SFR ($M_\odot$ yr^{-1})=L$_{\mathrm{H}\alpha}$/(6.93×10^{33} W), corrected to a Kroupa (2001) IMF in order to be consistent with SFRs reported in the SDSS catalogs. Then, by dividing by the area of the galaxy covered by each portion of the slit (e.g., for MMT, $1.25'' \times 0.3''N$, where N is the number of individual rows that went into each coadded spectrum), we estimate the SFR surface density as a function of position across each galaxy.

Stellar mass densities (μ_*) are derived for each individual spectral bin by re-measuring SDSS photometry through an aperture matched to each slit segment, and calculating stellar mass for that segment using the SED fitting procedure described in Wang et al. (2011a). Dividing by the area under the slit then yields μ_*, and we further calculate a local measure of specific star formation rate, sSFR, under each slit segment by dividing SFR surface density by these μ_* values.

We limit our analysis of stellar absorption features in this work to the $D4000_n$ index, which measures the strength of the 4000Å break (Balogh et al. 1999). This index is an indicator of stellar population age (see, e.g. Kauffmann et al. 2003a). We measure this index directly from the spectrum, but only include measurements from spatial bins where the continuum S/N around 4000 Å is > 5 (per Å).

When we compare our results with those derived from SDSS fiber spectra, we select all galaxies in SDSS Data Release 7 (Abazajian et al. 2009, hereafter, DR7) with redshifts in the GASS range ($0.025 < z < 0.05$). We make use of star formation rates, stellar masses, and metallicities provided in the MPA-JHU value added catalogs[13] We also use raw line fluxes from these catalogs for calculating metallicities as described in the next section.

We note that measurements of emission and absorption line strengths for all galaxies in the GASS spectroscopic sample will be made available online[14] upon completion of the survey.

3.1. *Metallicities*

To estimate gas-phase metallicities, we rely primarily on the O3N2 empirical index described by Pettini & Pagel (2004). This index relates two line ratios, [N II] λ6583/Hα and [O III] λ5007/Hβ to the metallicity of the ionized gas. All four of these emission lines fall within our spectral coverage for both MMT and APO spectra. As for the star formation rates, we first correct

---

[13] http://www.mpa-garching.mpg.de/SDSS/DR7/

[14] http://www.mpa-garching.mpg.de/GASS/

all four lines for extinction. However, because the index relies on ratios of lines that are quite near each other in wavelength, their sensitivity to extinction is negligible. We express gas-phase metallicities in the usual manner here, in terms of $12 + Log(O/H)$. The Pettini & Pagel (2004) relation is $12 + Log(O/H) = 8.73 - 0.32 \times O3N2$, where $O3N2 = Log(([\text{O III}]/H\beta)/([\text{N II}]/H\alpha)$. This relation is valid at least across the range $8.0 < 12 + Log(O/H) < 9.0$, which encompasses all of our measured metallicities.

The four lines that go into the O3N2 index are the same used in the classic Baldwin, Phillips & Terlovich (1981), or BPT, diagram used to discriminate emission from AGN from that due to star-formation. In Figure 2, we plot line ratios for all spatial bins from our sample, where all four lines are measured with $S/N > 5$. Points are color-coded according to the metallicity estimated using the O3N2 indicator, as illustrated by the color bar. The dashed line shows the division between galaxies with star-formation dominated and AGN-dominated or AGN/star-formation composite emission defined by Kauffmann et al. (2003b).

We exclude from our analysis any regions where the measured emission exhibits AGN-like line ratios, which are marked in black in Figure 2. Note that we choose a dividing line that is slightly offset (+0.1 dex in both axes) from that used by Kauffmann et al. (2003b), shown as a thick solid line in Figure 2. This is done in order to avoid throwing out star-forming points that fall just over the line due to statistical fluctuations. We thus include a small number of points with so-called 'composite' AGN and star-formation emission lines. These make up less than 10% of the total, and the fractional AGN contamination for points close to the star-forming sequence of the BPT diagram is low (Brinchmann et al. 2004), so their inclusion is not likely to bias our metallicity or star formation estimates in any significant way.

We note that the number of AGN points marked in Figure 2 is larger than the number of galaxies in our sample (180 points c.f. 174 galaxies). This is because AGN emission often extends into more than one spatial bin at the centers of our galaxies, where our bins tend to be only slightly larger than the typical seeing disk. In addition, a number of the non-star-forming galaxies in our sample exhibit faint, spatially extended emission with LINER-like line ratios, and these are also included on the diagram. In total, 47% of our galaxies exhibit central emission indicative of an AGN, in line with expectations for a population in this mass range (Kauffmann et al. 2003b). Approximately 10% of our galaxies have extended emission (beyond $3''$from the nucleus) with LINER-like line ratios.

At the lowest metallicities, it is clear from Figure 2 that [O III]/Hβ varies only slightly, and so the [N II]/Hα ratio alone is sufficient to determine metallicity. Likewise, in the intermediate metallicity regime, a lower limit on the [O III]/Hβ ratio sets an upper limit on metallicity even when Hβ is undetected. Spatial bins with upper limits on metallicity make up approximately 14% of the sample, and will be clearly marked in any figures where they are included.

To ensure the reliability of our O3N2-based metallicities, we have also calculated metallicities using the method described in T04. This Bayesian technique determines the most likely metallicity using information from all available emission lines, and so utilizes lines beyond the four considered so far, including the [O II] λ3727 doublet and the [S II] $\lambda\lambda$6717,6731 lines. As will be discussed in more detail in §4, we find that metallicities calculated in these two ways yield very similar results for metallicity gradients and their trends as a function of galaxy mass and type.

Despite the well-known disagreements in the overall metallicity scale exhibited by these and other metallicity indicators, recent work by Kewley & Ellison (2008) provides a series of tabulated functions that allows us to convert metallicities measured with one method onto the metallicity scale of another. To estimate the typical uncertainties on our metallicity measurements, we therefore convert our T04-style metallicities onto the O3N2 scale in order to make a direct comparison. We find that the rms difference in metallicities measured according to these two methods is ∼0.07 dex, which is comparable to the agreement quoted by Kewley & Ellison (2008). Except for metallicity upper limits and a small number with low S/N ($\sim 10\%$), the formal statistical uncertainties on our measurements are typically much smaller than 0.07 dex, with a median of only 0.01 dex. We will thus adopt 0.07 as a reasonable estimate of the uncertainty in all of our metallicity measurements.

For the subset of galaxies observed with the Apache Point telescope, we have access to a broader spectral range which allowed us to compare metallicities derived from O3N2 to those derived using the R23 index (following Kobulnicky & Kewley 2004) which utilizes [O II] λ3727 in addition to [O III] λ5007. After adjusting for systematic differences between the two metallicity scales (Kewley & Ellison 2008), we find that the two indicators are in agreement with an rms difference of approximately 0.15 dex.

Finally, we note that variations in the N/O ratio in galaxies have been shown to bias both O3N2 (Pérez-Montero & Contini 2009) and T04 (Yin et al. 2007) metallicities, in the sense that emission line regions with high N/O ratios tend to have their metallicities overestimated compared to so-called direct-T_e based metallicities. However, this bias sets in at different thresholds in N/O for O3N2 compared to T04. Thus, if elevated N/O ratios were a significant source of bias in our sample, we would expect to see divergence in the O3N2 and T04 metallicities for some fraction of points where the N/O ratio is in between the two thresholds. Given the very good agreement of 0.07 dex mentioned above, we conclude that variations in N/O ratio are not a significant source of bias in our sample.

4. RESULTS

In the left panel of Figure 3, O3N2-derived metallicities for all 1298 measured points (excluding AGN) in the 151 galaxies in our sample of star-forming galaxies are plotted as a function of radius normalized by R_{90} (R/R_{90}). We adopt a logarithmic x-axis for clarity, since our adaptive binning technique yields a large number of narrow bins at small radius and a comparatively smaller number of wide bins at high radius. We include all measured metallicities with nominal 1-σ statistical uncertainties of < 0.15 dex. As discussed above, only $\sim 10\%$ of these points have statistical uncertainty higher than our typical

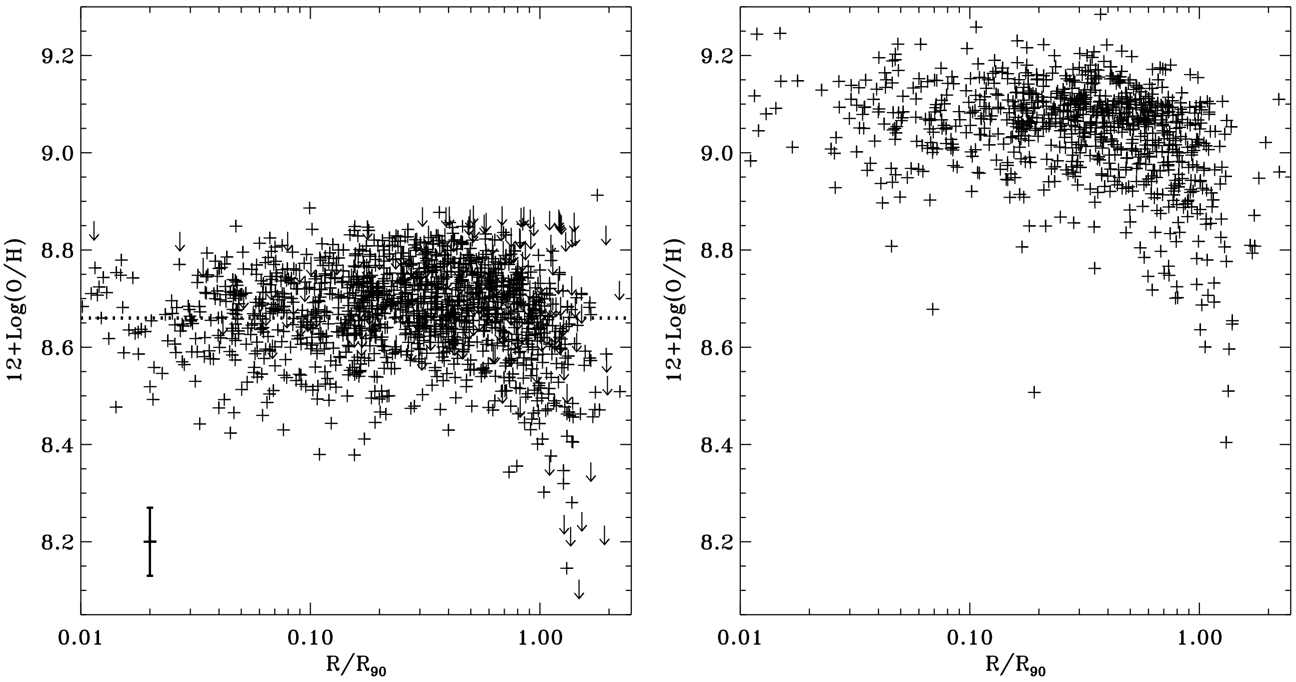

Figure 3. Gas-phase metallicities as a function of radius, R/R_{90}, for all spatial bins in all galaxies in our sample. Metallicities are estimated from the Pettini & Pagel (2004) O3N2 index (left), and from the method of T04 (right). Black crosses show metallicities with nominal 1-σ statistical uncertainties of < 0.15 dex (left, $n = 1298$) or < 0.18 dex (right, $n = 828$), respectively. In the left-hand panel, downward-pointing arrows denote upper limits in cases where not all emission lines were measurable ($n = 182$). Our typical uncertainty of 0.07 dex is illustrated by the error bar at lower left.

systematic uncertainty of 0.07 dex. Downward pointing arrows indicate upper limits for 182 points where not all emission lines were measurable. In the right-hand panel, we plot metallicities determined via the T04 method, this time including all 828 points with an uncertainty from the Bayesian analysis of < 0.18 dex.

The large systematic offset between metallicity indicators is dramatically clear from Figure 3, but the difference in scales is as expected from the conversion formulae given in Kewley & Ellison (2008). Of more importance are the two key features that both panels of Figure 3 have in *common*. First, we note that the vast majority of points are clustered in a narrow range of metallicity, which on the O3N2 metallicity scale is very near the solar value of $12 + Log(O/H) = 8.66$ (Asplund et al. 2004, marked as a dotted line). That is, the radial profiles appear quite flat across most of their range. Second, both panels of Figure 3 feature a significant drop in metallicity for some points located at large radius ($R > 0.7R_{90}$). This means that in some galaxies, gas-phase metallicity drops precipitously as one approaches the edge of the visible galactic disk. Thus, although the absolute metallicity scale differs quite a lot—note, in particular, that most galaxies appear to feature metallicities $> 2\times$ solar abundance on the T04 scale —we find that the *relative* metallicity profiles derived using both methods are very similar. In the following, we will examine both key features of these profiles in more detail.

4.1. *Inner Metallicity Profiles*

Let us first consider the inner metallicity profiles ($R < R_{90}$); we will discuss the outer metallicity drops in more detail below. The fact that metallicities appear essentially flat out to nearly R_{90} for the GASS sample may seem somewhat surprising. Previous work on galaxy metallicity gradients (Zaritsky et al. 1994; Moustakas et al. 2010) feature a diverse array of gradients, with some being flat, but many others exhibiting steady declines toward higher radius. Though their total sample sizes are smaller, and their galaxies are selected differently from ours, we might expect to see at least some galaxies with declining gradients.

To examine whether plotting all points on a single plot might be obscuring the presence of a sub-population of galaxies with declining metallicities, Figure 4 shows metallicity as a function of radius divided into four bins of host galaxy stellar mass. We now use a linear rather than a logarithmic scale in R/R_{90} in order to highlight trends in the inner region of the galaxy. It seems that galaxies in the lowest mass bin *do*, on average, exhibit significant metallicity gradients, where the Spearman's rank correlation coefficient, ρ, between R/R_{90} and $12 + Log(O/H)$ is modest at $|\rho| = 0.34$, but still significant at the 5σ level. In contrast, metallicities in the higher mass bins appear to be quite flat as a function of radius, and show no statistically significant deviation from zero slope.

In the Appendix, we plot the individual radial profiles of the 100 galaxies with ≥ 8 measured points, arranged in order of ascending stellar mass. From these, one can verify that most inner gradients are flat, but a minority do have sloping gradients. The distribution in stellar mass of these sloping gradients is hard to discern from the plots, but we can attempt to quantify this further.

In general we prefer to avoid quoting gradients in terms of a single number, e.g., dex of decline per R_{90}, because not all profiles are well fit by a straight line. Nevertheless, we have performed these crude linear fits, and plot in Figure 5 the best-fit slope to each galaxy gra-

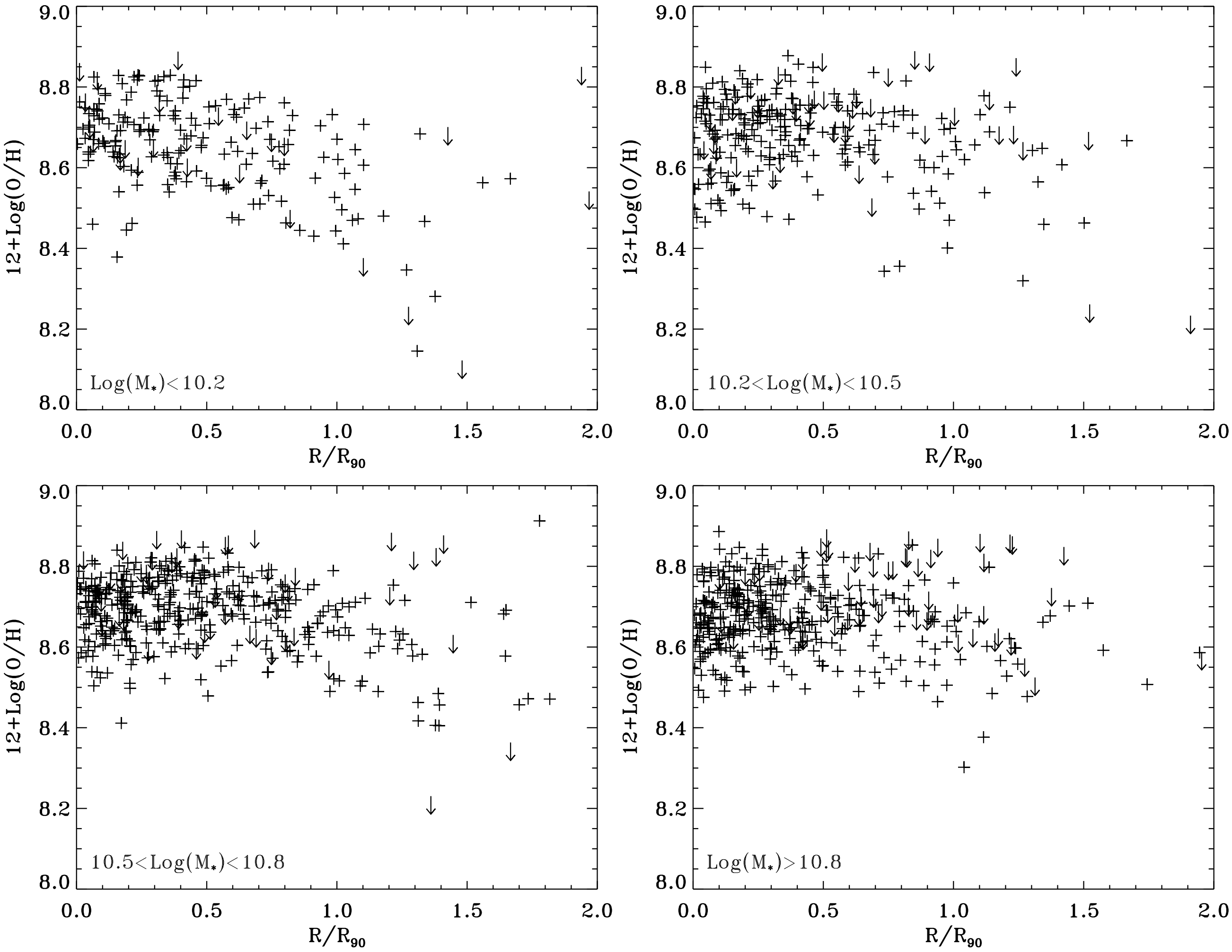

Figure 4. Metallicity versus radius (R/R_{90}) for all spatial points divided into four bins of galaxy stellar mass, as marked below each plot. While low metallicity points in the outer disks are found in all bins, only galaxies with Log(M_*) < 10.2 exhibit metallicities that clearly decline with radius on average.

dient as a function of stellar mass, stellar mass density (μ_*), and concentration (R_{90}/R_{50}), limited to the 100 galaxies shown in the Appendix. We plot slopes derived from a linear least-squares bisector fit. We used the IDL astronomy library routine SIXLIN, which performs fits with six different linear regression methods (Isobe et al. 1990), to examine how robust the slopes are to varying the fitting method. We find that slopes derived using different methods have typical rms agreements of only ± 0.15 dex/R_{90}, which is comparable to the scatter in the derived gradients at fixed M_* shown in Figure 5.

Despite the high uncertainty, it seems that most of the objects with plausibly declining gradients (≤ -0.1 to -0.2 dex per R_{90}) occur in the lowest stellar mass galaxies in the GASS sample, consistent with the average profile in Figure 4. Since low-mass galaxies also tend to have low stellar mass densities and concentrations, it is not surprising that declining gradients also occur preferentially at low μ_* and concentration. The formal Spearman rank correlations are small ($|\rho| \sim 0.3$) but statistically significant for stellar mass and concentration, while that for μ_* is marginal.

Bar fractions have also been measured for face-on galaxies within the GASS sample (Wang et al. 2011b), but only a small number of galaxies studied here (~ 10) unambiguously contain bars; those that we identify do not show any clear difference in metallicity gradient from the overall sample, but better statistics will be needed to draw any meaningful conclusions.

While we are unable to say whether morphological characteristics (e.g., concentration) or galaxy mass is more important in setting the slope of galaxies' metallicity gradient, our results nevertheless suggest that declining gradients are more frequently found in galaxies below some threshold in stellar mass and/or concentration (i.e., late-type morphology), which is consistent with the results of Vila-Costas & Edmunds (1992).

To return to our original question, then, could this apparent threshold explain why earlier samples seemingly contain a higher incidence of galaxies with declining gradients? To check, we have re-examined the 21 SINGS sample galaxies with metallicity gradients presented in Moustakas et al. (2010). By eye examination reveals that 8 have unarguably declining gradients, 7 have seemingly flat gradients, with the remainder ambiguous. We then estimate the stellar masses of these galaxies via a simple scaling of their K-band luminosities by a mass-to-light ratio set by their B–V colors

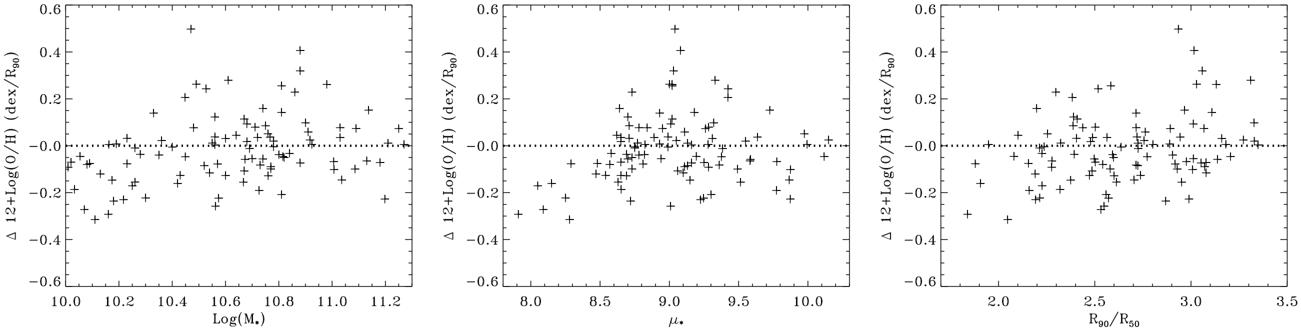

Figure 5. Metallicity gradient in terms of dex per R_{90} for each of 100 galaxies with greater than 8 measured points, plotted versus stellar mass (left), average stellar mass density (middle), and concentration (right). Gradients are measured using a linear least-squares bisector fit. Uncertainty is estimated to be 0.15 dex, and so galaxies with significantly declining gradients occur predominantly at the lowest masses, mass densities, and concentrations in the GASS sample.

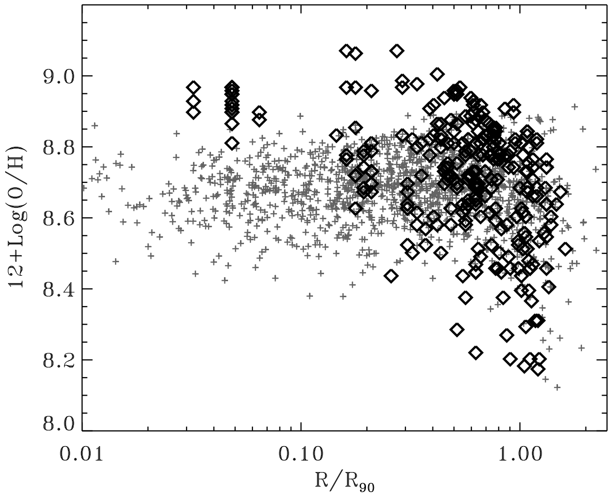

Figure 6. Metallicity versus R/R_{90} for the massive (Log($M_* >$ 10)) galaxies in the SINGS sample (open diamonds), compiled by Moustakas et al. (2010), including only galaxies with $>$ 8 measured metallicity points. R23 metallicities have been converted to the O3N2 scale using the formula in Kewley & Ellison (2008), and radii reported in terms of the D_{25} radius have been scaled to an R/R_{90} scale assuming the median relation $R_{90} = 0.6 * (D_{25}/2.)$. GASS points are plotted underneath as grey crosses.

($Log(M/L_K) = -0.56+0.135(B-V)$) (Bell et al. 2003), corrected to our Kroupa IMF. We find that 5 out of 8 galaxies with declining gradients have Log(M_*) $<$ 10.2, while 5 out of 7 with flat gradients lie above this mass. Similarly, the most luminous galaxies in the sample of Garnett et al. (1997) appear to have quite flat gradients as well.

This is suggestive, but we would ideally like to compare gradients from the literature more directly with our sample, in particular for galaxies falling within the GASS mass range. Moustakas et al. (2010) have made available electronically a compilation of points with metallicity measured on the R23 system. We have obtained this data, and we use the Kewley & Ellison (2008) formula to convert to the O3N2 system. Moustakas et al. (2010) recorded the positions of individual metallicity points in terms of the D_{25} optical radius, which differs from our chosen R_{90}. We use the subsample with SDSS coverage to estimate that $R_{90} = 0.6 * (D_{25}/2.)$.

In Figure 6, the converted SINGS points are plotted versus radius, as open diamonds. We include only points from the 15 SINGS galaxies with $Log(M_*) > 10$ and > 8 measured points, and for comparison we plot our GASS points from Figure 3 as small circles. First, we note that the SINGS points from these high-mass galaxies are in quite good agreement with our own across most of the radial range probed, including the drops we observe at high radius. However, SINGS data in some cases appear to reach higher metallicities at the centers of galaxies, compared to our own.

Since GASS probes more distant galaxies, features on spatial scales of $< 0.1R/R_{90}$ begin to fall below the resolution of the data, and one might worry that we bin over too large an area to detect these elevated central metallicities. This could contribute to the overall flatness of the gradients we see. However, SINGS galaxies exhibit high-metallicity at radii as large as ~ 0.3 R/R_{90}, beyond the regime where limited spatial resolution could be affecting the GASS measurements.

Similarly, one might worry that the difference arises because Moustakas et al. (2010) compiled measurements of isolated HII regions, while our data are integrated over a broader area, and so may include a component from the diffuse ionized medium associated with older star formation or shock-ionized gas (e.g., Dopita et al. 2006). However, within the regime spanned by our data, Dopita et al. (2006) showed that the bias between measurements of HII regions and whole galaxies is small, and we calculate that it would lead to a metallicity offset of < 0.03 dex, smaller than the offset observed, and less than half our quoted uncertainty.

We suspect, instead, that the slightly higher SINGS points are either an artifact of the conversion formula used to place SINGS data on the O3N2 scale, or else a reflection of the inherent limits to uniformity in any literature compilation like Moustakas et al. (2010). First, we note that these high metallicity points ($12+Log(O/H) >$ 8.95) lie outside of the full range of metallicities used by Kewley & Ellison (2008) in deriving their conversion formula, and so the conversion from the original R23 to our O3N2 for these points is at least a mild extrapolation. Furthermore, the highest SINGS points at $12 + Log(O/H) > 8.95$ belong almost entirely to two galaxies, NGC3351 and NGC5194 (M51), hinting that systematic offsets between literature sources could be important.

In general, however, our new results on the large, unbiased GASS sample, are in good agreement with previ-

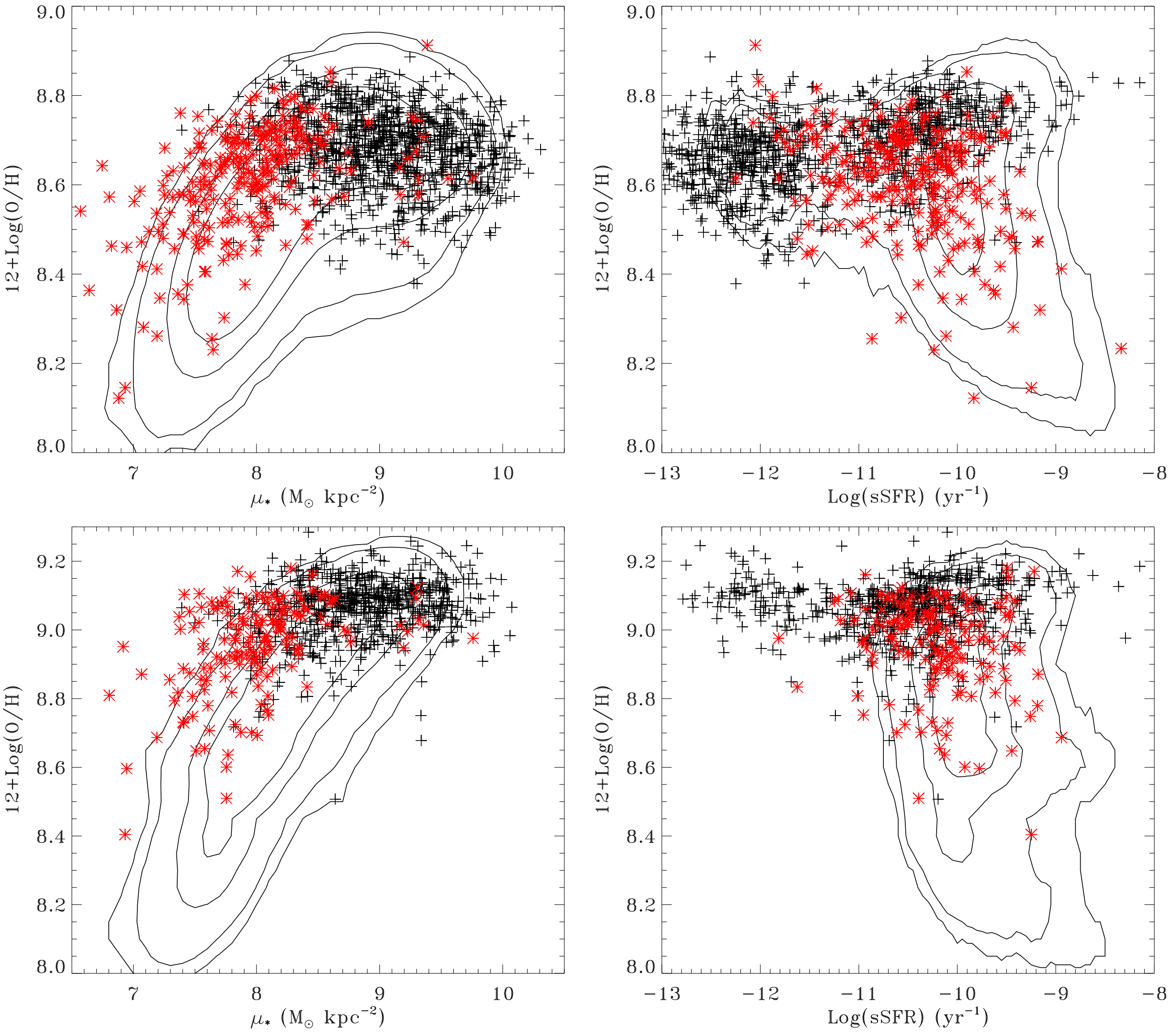

Figure 7. **Left:** Metallicity versus projected stellar mass surface density (μ_*), for all independent spatial bins within $0.7R_{90}$ (black crosses) and outside $0.7R_{90}$ (red asterisks). Top panel shows O3N2 metallicities, while bottom panel shows T04 metallicities. Contours show where 33%, 67%, 95% and 99% of SDSS galaxies in the same redshift range lie (including all stellar masses), where μ_* and metallicity are for the region directly under the central $3''$fiber. The μ_*–metallicity relation for SDSS galaxy centers is similar to that for GASS galaxies, but exhibits a slightly different downturn. **Right:** Metallicity versus dust-corrected specific star formation rate (sSFR), with symbols and contours coded as before, and again with O3N2 metallicity in top panel and T04 in bottom. Low metallicity regions in galaxy outskirts exhibit increasing sSFR with decreasing metallicity. Lack of contours at low sSFR in the bottom panel is a selection artifact, as T04-style metallicities are not reported in the MPA/JHU catalogs for such low star formation rates.

ous work, but fill in the picture with a more complete sampling of the full radial range. Though a more robust investigation of how metallicity gradients vary with mass must await more data extending to lower masses, we have shown in this Section that galaxies at high masses have predominantly flat inner metallicity profiles, and that this result is not in conflict with earlier work once we compare within the same stellar mass range.

4.2. *Outer Metallicity Drops and the μ_*-Metallicity Relation*

Having established that inner metallicity profiles are largely flat except for those near the low end of our mass range, we wish to understand why some galaxies appear to show precipitous drops in metallicity at or near R_{90}. First, we note that galaxies with these steep metallicity drops occur in galaxies of all stellar masses: low metallicity points can be seen at large radius in all four stellar mass bins plotted in Figure 4. In asking what might be driving these drops, we must first characterize them in two ways: first, what types of galaxies do these low-metallicity regions reside in, and, second, what are the internal, local conditions like at each of these low-metallicity sites? In this section, we will examine the link between outer metallicity and *local* properties within the galactic disk, and defer the question of global galaxy properties to §5.

In Figure 7, we plot metallicity as a function of local stellar mass density (μ_*, left panels) and specific star formation rate (sSFR, right panels). Results are shown for both the O3N2 (top) and T04 (bottom) metallicity calibrations. Interestingly, the μ_*–metallicity relation evaluated *within galaxies* bears striking resemblance to the well-known global mass-metallicity relation (e.g., T04). There is a relatively tight correlation between metallicity and local surface density at μ_* less than $3\times10^8 M_\odot$ kpc^{-2} ($|\rho| = 0.38$, 8.5σ), followed by a "turnover" where the dependence of metallicity on stellar surface mass density weakens, similar to the way the global mass–metallicity relation flattens at high masses.

In Figure 7, data marked with red asterisks are from regions with $R > 0.7R_{90}$. It is clear, therefore, that low metallicity regions in the outskirts of galaxies are generally associated with *low* underlying stellar mass density. Likewise, in the right-hand panel of Figure 7, one can see that in the outer disks the lowest metallicity regions tend to be those with the highest ratios of current star formation to pre-existing stellar mass (i.e., sSFR).

As in the μ_*-metallicity relation, points closer to the centers of galaxies do not show a significant correlation between sSFR and metallicity. Of course, this was expected given that inner metallicities are nearly invariant, as discussed above, but it is still interesting to note that sSFR in these inner regions spans four orders of magnitude without appreciably affecting metallicity.

The contours overplotted in Figure 7 show where SDSS galaxies in the GASS redshift range (but spanning all stellar masses) lie on these relations. Recall that for these galaxies, μ_*, metallicity, and sSFR pertain to the central regions of the galaxies falling directly under the SDSS fiber. We find that the central regions of SDSS galaxies also follow a similar μ_*–metallicity relation, but there is a somewhat sharper decline in metallicity with decreasing μ_*, or perhaps a shift in the threshold value of μ_* where metallicity begins to decline, compared to the outskirts of GASS galaxies.

Since the low-metallicity points in the SDSS sample come from the centers of galaxies with much lower stellar masses than the GASS sample, it may not be surprising that the two relations differ slightly. Specifically, one standard explanation for the mass-metallicity relation says that low mass galaxies exhibit lower metallicity because a higher fraction of their metals are driven by supernovae winds out of the galaxy due to their shallower potential wells (T04; Dalcanton 2007). Since even the outskirts of our massive GASS galaxies have higher escape velocities than the centers of low-mass ($\sim 10^9 M_\odot$) galaxies, such an effect could be responsible for the downward offset of these galaxies' centers relative to the relation that we see. Other explanations are also possible, including a secondary dependence on sSFR similar to that advocated by Mannucci et al. (2010), but a fuller exploration is beyond the scope of this paper.

Regardless of the source of the offset, the fact remains that our outer disk resolved points occur in very different locations within galaxies of very different masses than the SDSS sample, but show a broadly similar relation between metallicity, stellar mass density, and specific star formation rate. One possible explanation is that the correlation between metallicity and local stellar surface density is more fundamentally a correlation between metallicity and local gas mass fraction (μ_g/μ_*). In regions of low μ_*, gas mass fractions are likely to be high (either at the centers of low-mass SDSS galaxies or the edges of high-mass GASS spirals), and the lower metallicities could be reflecting a less complete processing of the gas into stars. Since one of the key strengths of the GASS sample is that we have direct measurements of the gas content, we are in a unique position to test whether subsolar metallicities and elevated sSFRs at our galaxies' outskirts are linked to their reservoirs of gas.

5. DISCUSSION

5.1. *The Relation Between Gas Content and Metallicity*

In C10, we found that the HI content of a given GASS galaxy was most accurately predicted by an fundamental-plane style "HI plane" constructed from whole-galaxy measurements of μ_* and NUV$-r$ color (which is a good proxy for sSFR). Since we have seen in the above section that local μ_* and sSFR are also tied closely to the local gas-phase metallicity, it is natural to wonder if we can identify a direct link between metallicity and gas content.

Remarkably, as can be seen in Figure 8, we have found that there is a surprisingly tight relation between the global HI fraction ($f_{HI} = M_{HI}/M_*$) and the lowest metallicity point that we measure ($R > 0.7R_{90}$, O3N2 scale) for each galaxy. We measure a correlation coefficient $|\rho| = 0.53$, significant at the 5σ level. We include upper limits as if they were detections for this calculation, but excluding these limits—either in f_{HI}, metallicity, or both—does not significantly change the result.

The C10 HI plane can be used to predict f_{HI} with rms accuracy of ~ 0.3 dex, and for comparison the scatter in our outer metallicity-f_{HI} relation is 0.4 dex in f_{HI}. We note, however, that outer metallicities that are near solar provide little predictive power for HI. In contrast, low metallicity points *do* seem to be universally associated with gas-rich galaxies. Whether or not Figure 8 reflects a *continuous* relation between outer metallicity and f_{HI}, or whether it is more properly described as a *threshold* in f_{HI}, above which outer metallicities are suppressed in proportion to the gas content, is unclear from the current data. We hope to revisit this issue with the full GASS data-set once it is in hand.

The quantity plotted in the left panel of Figure 8, being defined as the lowest metallicity we measure in a galaxy's outskirts, could be subject to a number of biases due to the imprecise definition. To check whether the way we define the metallicity value is driving this relation in any way, we also calculated metallicity values by coadding all spectroscopic flux from $R > R_{90}$ into a single high-S/N spectrum for each galaxy. Metallicities measured from these spectra, being integrated over a much larger area of the galaxy, often do not reach such low values as our more finely sampled points. Even so, when plotting these metallicity values against f_{HI}, in Figure 8, right panel, we find a nearly identical relation as before, with a marginally higher $|\rho| = 0.57$ and 6σ significance. We note, also, that plotting the size of the outer metallicity *drop*, rather than the outer metallicity directly, gives largely the same results. Considering that the inner metallicities of most GASS galaxies are nearly solar everywhere, this is not surprising.

To understand what might be driving this peculiar re-

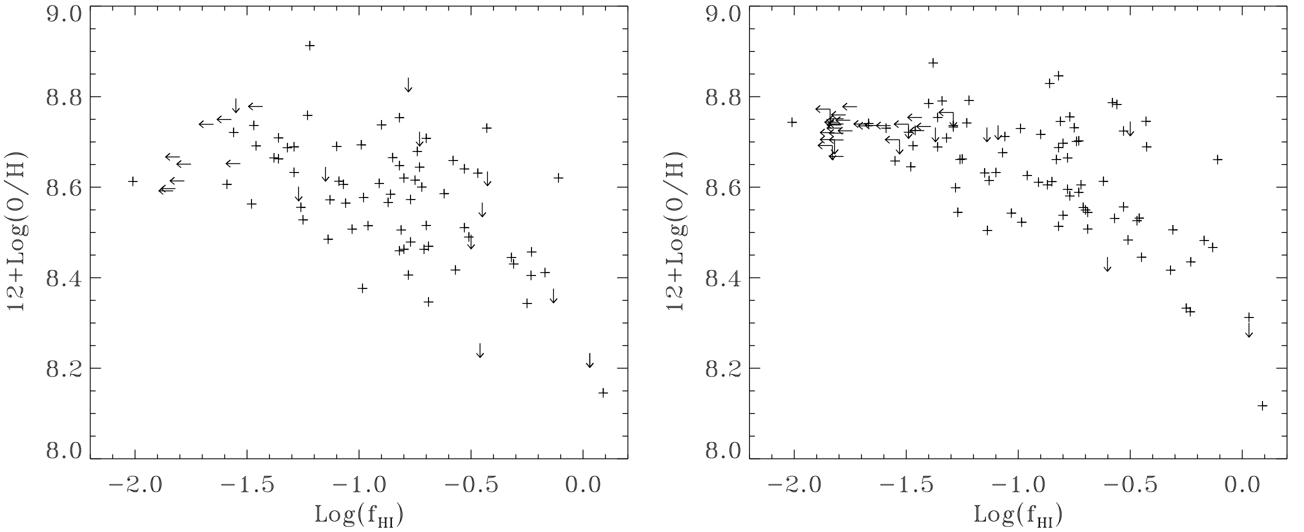

Figure 8. Galaxy outer disk metallicity as a function of total galaxy HI fraction, f_{HI}. Left-hand panel displays the lowest-measured metallicity point for each galaxy, while the right hand panel shows metallicities measured from the integrated spectrum of all flux from $R > R_{90}$ for each galaxy. Both show that outer-disk metallicity is well-correlated with total HI content.

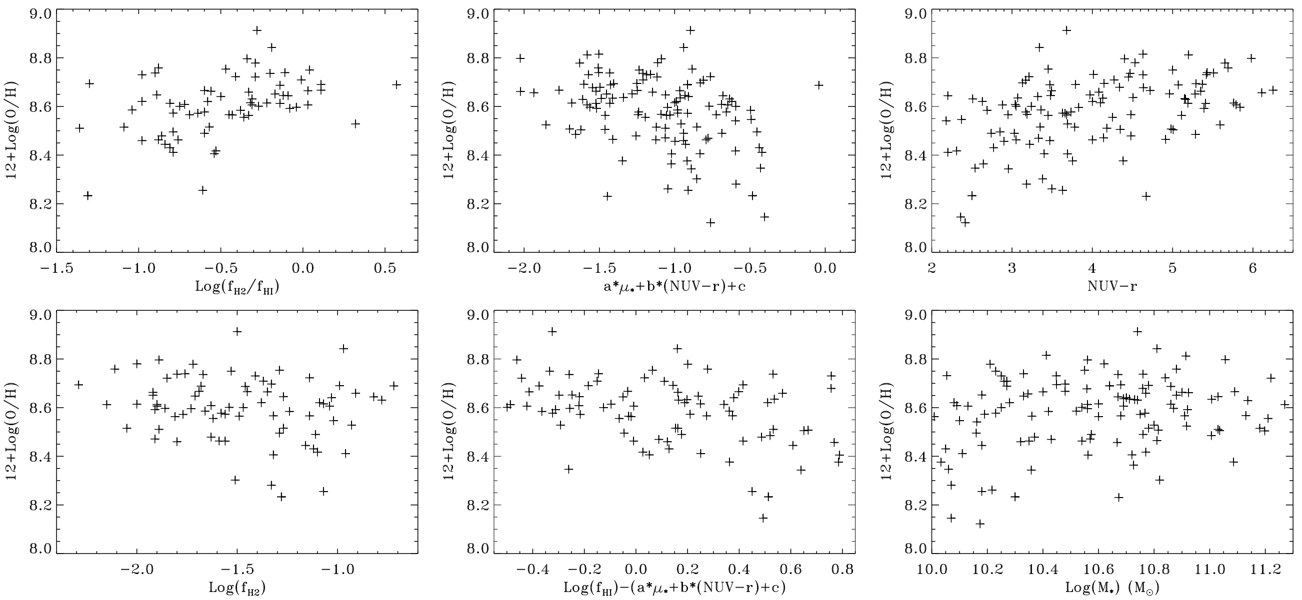

Figure 9. Outer metallicity, calculated as in the left panel of Figure 8, plotted as a function of, from top left to bottom right, ratio of molecular to atomic gas (f_{H2}/f_{HI}), the combination of NUV−r and full-galaxy μ_* found to best predict HI content by C10, NUV−r color alone, molecular gas fraction (f_{H2}), residuals from the C10 HI plane, and stellar mass (M_*). None predict outer metallicity as well as the HI fraction (f_{HI}) alone.

lation between a very *local* quantity, the outer metallicity, and the *global* gas content, we must examine how outer metallicity relates to other global galaxy characteristics. In Figure 9, we plot the minimum outer metallicity on the O3N2 scale (as in the left panel of Figure 8), as a function of several such quantities.

The first quantity of interest is the molecular gas fraction, f_{H2}. As can be seen in the lower-left panel, f_{H2} by itself does not correlate with outer metallicity. Since H_2 is generally more centrally concentrated in galaxies than HI (e.g., Leroy et al. 2009), this result may not be surprising. In fact, we do detect a weak correlation ($|\rho| = 0.39$, 3.9σ) between f_{H2} and *central* metallicity. The outer metallicity may simply be more closely associated with the size of a galaxy's gas *reservoir*, as traced by HI, rather than by the amount of currently star-forming gas, traced by H_2.

Interestingly, the *ratio* of molecular to atomic gas, shown in the top left panel, *does* correlate with outer metallicity, in the sense that galaxies more dominated by their HI exhibit lower outer metallicity. However, this correlation is weaker ($|\rho| = 0.44$) and less statistically significant (3.7σ) than the HI relation in Figure 8, and so we may only be seeing here a reflection of the underlying relation between HI and outer metallicity.

In the upper middle panel of Figure 9, we plot outer metallicity as a function of the same combination of global NUV−r and μ_* that goes into the C10 HI plane–

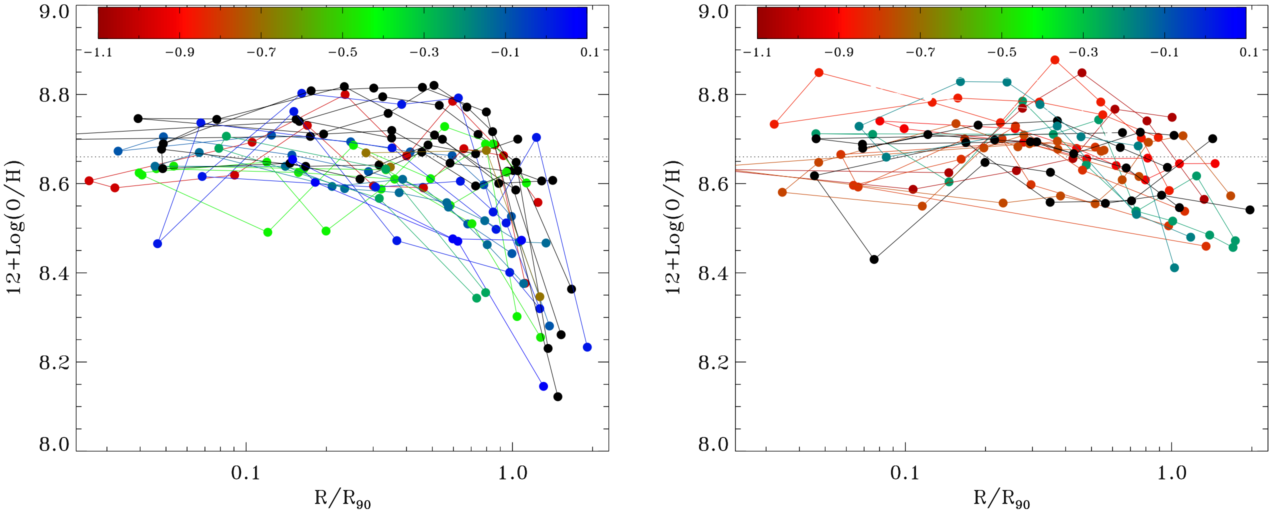

Figure 10. Left: Metallicity versus R/R_{90} for the 13 galaxies with the largest outer metal drops. Right: Metallicity versus R/R_{90} for the matched comparison galaxies. In both panels, solid lines connect adjacent measurements for each individual galaxy, and both halves of each galaxy are plotted separately, 'folded' onto the same R/R_{90} scale. Points and lines are color coded for galaxy HI content, according to the color bar at top, which indicates $Log(f_{HI})$ associated with each shade. Galaxies that do not yet have an HI measurement are plotted in black.

i.e., the x-axis can be thought of as the f_{HI} that is predicted given the galaxy's NUV−r and μ_*. We do this to evaluate the possibility that the f_{HI}–metallicity relation is simply an induced correlation: if it is really the star formation rates and stellar mass densities that set metallicity, as our results above seem to suggest is true locally, it may be that the correlation with HI content is not fundamental, but instead driven by the dependence of HI on the same underlying parameters (sSFR and μ_*, but galaxy-averaged now) that drive metallicity.

What the upper middle panel of Figure 9 shows, however, is that the correlation of outer metallicity with global μ_* and NUV−r is relatively weak compared to Figure 8, with $|\rho| = 0.37$ and a significance of 4σ. Since C10 found the relation between f_{HI} and NUV−r color alone was nearly as tight as the one including μ_*, we also plot in the upper right panel outer metallicity versus NUV−r. The correlation here is more significant, at 4.8σ, but again the correlation coefficient is not quite as strong ($|\rho| = 0.44$) as we saw in Figure 8.

The *residuals* from the C10 HI plane are useful for identifying galaxies that have either abnormally high or low atomic gas content, compared to that expected for galaxies with their specific combination of μ_* and NUV−r. In the lower middle panel of Figure 9, we plot these residuals versus outer metallicity. The correlation is quite low and only marginally significant (2.8σ), suggesting that it is the absolute level of HI content that matters, rather than the *excess* or *deficit* of HI compared to other similar galaxies.

Finally, we checked for relations between metallicity and other global galaxy properties such as concentration, μ_*, and M_*. None show any significant correlation; the lower right panel of Figure 9 shows metallicity versus Log(M_*), which is representative of the others. Outer metallicity thus appears to depend hardly at all on the structural properties of galaxies in GASS.

In short, we have found that the relation between f_{HI}, a global property of the galaxy, and outer metallicity $12 + Log(O/H)$, a very local one, is tighter and therefore likely *more* fundamental than any relation between global SFR/μ_* and metallicity. The question, then, is why this should be true. One possibility is that metallicity at the outer edge of the star-forming disk is simply a sensitive 'thermometer' of sorts for measuring the amount of new gas accreting onto the disk of the galaxy, or perhaps for the rate that existing gas is transported inward. Lower metallicities would simply be reflecting a higher proportion of pristine or relatively unenriched gas residing in or flowing through the outer stellar disk.

If this is correct, then varying rates of gas accretion/flow may leave other signatures in, for example, the stellar populations and star formation rates of galaxies, or on their radial gradients. To evaluate this possibility, in the following section we will examine in detail the subset of galaxies exhibiting the strongest metallicity drops in our sample, and compare to a control sample selected without regard to outer metallicity.

5.2. *The Galaxies with Steepest Metallicity Drops*

In order to determine whether a low outer metallicity is associated with any distinctive features in the star formation rates and histories of our galaxies, either at their outer edges or across their disks, we select for detailed study a small sample containing only those galaxies with the steepest drops in outer metallicity. We will refer to this as the 'low metallicity' or 'large drop' sample, and we will compare it to a 'control' sample selected without regard to metallicity, but matched in global characteristics one-for-one with galaxies in the large-drop sample. We note that both samples are selected from the subset of 119 galaxies that exhibit measurable star formation in their outskirts at $R > 0.7R_{90}$, which ensures that all the galaxies in the control sample have significant star formation and measurable metallicities at the same large radii as the large-drop galaxies.

In total, we identify 13 galaxies with outer-disk metallicities $12 + Log(O/H) < 8.4$, a threshold we chose both because no measured point in the inner region of any galaxy reaches this low, and because it is significantly be-

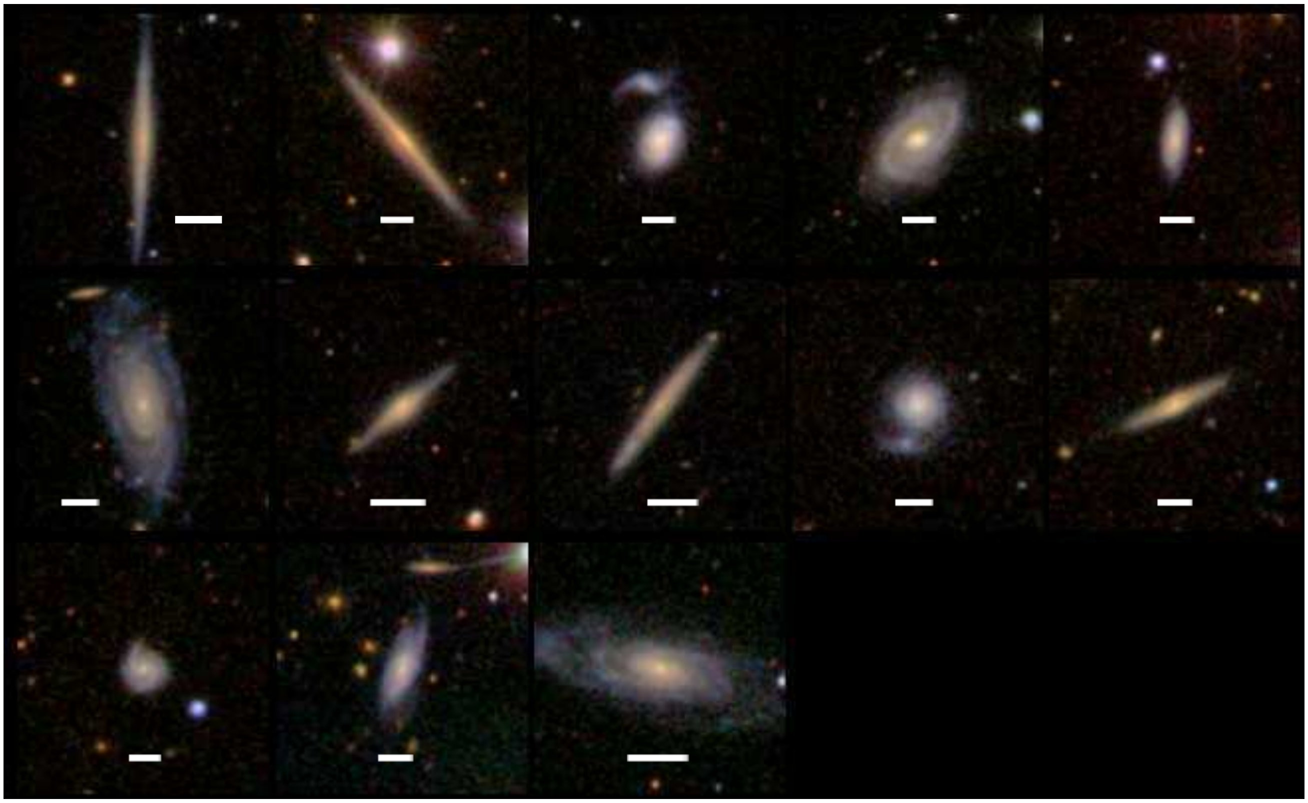

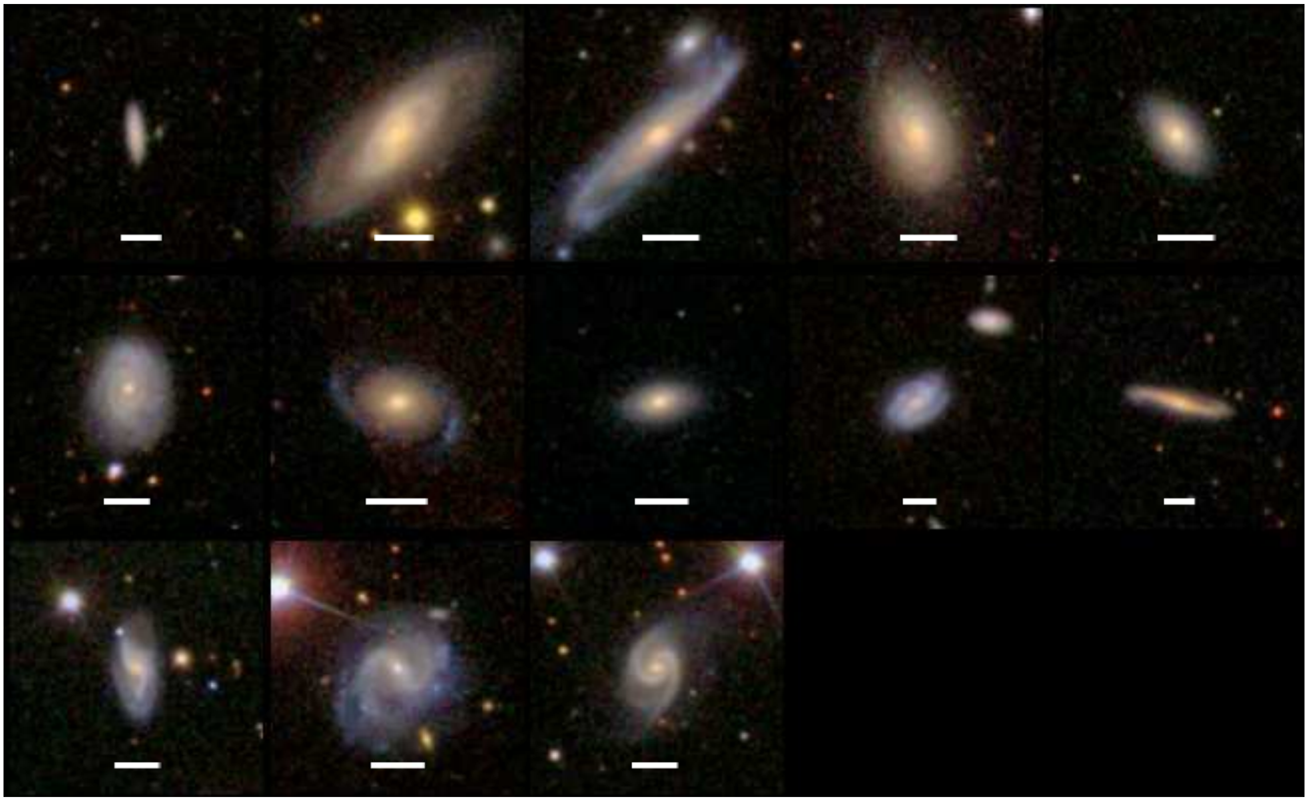

Figure 11. SDSS postage stamp images of galaxies with the steepest outer metallicity drops (top), and the matched control sample selected without regard for metallicity (bottom). Images are $80'' \times 80''$, and are arranged so that the match to a galaxy in the top panel is in the same relative position in the lower panel. White bars in each image indicate a projected physical length of 10kpc at the redshift of that galaxy.

low solar at the $> 3\sigma$ level (0.25 dex). Such galaxies make up about 10% of the total sample, and so even though the number identified is small, they represent a significant proportion of all massive star-forming galaxies. For the control sample, we select each matched counterpart by requiring that it be within 0.2 dex in stellar mass, 0.4 dex in global μ_*, and 0.3 in NUV-r color, similar to the procedure in Wang et al. (2011a). These limits were chosen to ensure that each large-drop galaxy has at least one match within our spectroscopic sample, and for cases with more than one match we select randomly among the choices.

In Figure 10, in the left-hand panel we plot the radial metallicity profiles of all 13 of our low-metallicity galaxies, as a function of R/R_{90}. Solid lines connect adjacent points to more easily follow the two folded halves of each profile (i.e., from both sides of each galaxy). Points are color coded for galaxy HI content, as illustrated by the color bar. It is clear from this plot that even those galaxies with the strongest metallicity drops show typically flat profiles in their inner regions (though some variation can, indeed, be seen). The median difference between the inner metallicity and the lowest measured point is ~ 0.3 dex for these objects. In the right-hand panel of Figure 10, we now plot the metallicity profiles of the control sample. Again, we see quite flat inner profiles, though there may be a hint that even these galaxies show subtle drops in metallicity at the highest measured points. Consistent with the overall correlation shown in Figure 8, galaxies with large metallicity drops have on average higher f_{HI}, which can be seen by noting the quite different range of colors between the two panels.

5.2.1. *Morphologies*

Our low-metallicity and control samples of galaxies by design have certain features in common, in particular their stellar masses and colors, as well as widespread star-formation extending out to $R > R_{90}$. Yet the disparity in the magnitude of the metallicity drop, as well as the wide variation in HI content, suggests that it is worthwhile to examine the images of both samples directly, to check for any subtle structural differences between the two that are not apparent when considering just the broadest characteristics.

In Figure 11, we show SDSS postage stamp images of these galaxies, with large-drop galaxies in the top panel, and the control galaxies at bottom. Images are arranged so that each matched pair of galaxies is in the same relative location in the top panel and bottom. We remind the reader that galaxy pairs were not matched in redshift (beyond the normal GASS constraint of $0.025 < z < 0.05$), so differences in apparent size are to be expected. For aid in comparison, white bars beneath each image indicate 10kpc projected distance at the redshift of each galaxy.

The first striking feature of Figure 11 is the large number of relatively edge-on galaxies in the low-metallicity sample. There are two possible explanations for this trend, both related to observing geometry. First, if the lowest metallicity regions are distributed unevenly, in a stochastic manner around the outer edges of galaxy disks, then an edge-on galaxy may afford us a higher probability of actually observing one, as the light collected by our slit has passed through a larger proportion of the galaxy. As can be seen in the Appendix, where individual profiles of large-drop galaxies are shown, some of these galaxies (but not all) show a metallicity drop on one side only, which might argue in favor of this scenario.

Alternatively, surface brightness enhancement due to viewing the galaxy edge-on could simply enable our fixed-integration time observations to reach further out in an edge-on galaxy, where such low-metallicity star-forming regions are perhaps more likely to reside. We do note that the maximum radius reached for edge-on galaxies is somewhat higher than for other objects (median of $1.2R_{90}$ for $b/a > 0.5$ vs $1.4R_{90}$ for $b/a < 0.5$), but it is unclear if this difference is large enough to cause the observed bias. The median radius reached for the control sample galaxies is only slightly lower than the large drop galaxies: $1.2R_{90}$ and $1.3R_{90}$, respectively.

A few galaxies in Figure 11 seem to harbor close-in tidally disturbed companions, which could suggest that new gas accreted or cannibalized from these companions is the source of the low-metallicity material. However, the majority of the large-drop galaxies do not have obvious companions, and the frequency of companions is not obviously larger than that seen in the control sample images. Indeed, the one large-drop galaxy that we have previously studied in detail (Moran et al. 2010), shows remarkably little evidence for any sort of dynamical disturbance, such as one would expect in the case of an accreted companion. Though beyond the scope of this paper, rotation curves are available for all of these galaxies, and we expect to address the relation between gas content and galaxy dynamics and/or mergers in a future paper.

We measured a number of quantitative morphological parameters for both sets of galaxies to search for any differences. These included asymmetry, bar fraction, and an asymmetry variant weighted to the outer disk (Wang et al. 2011b). Though such small samples make it difficult to assess any statistical difference between the two sets of galaxies, we find no clear evidence that the populations are different in any of the key morphological measures. This remains true whether or not we exclude the most edge-on galaxies (which could have peculiar values of these morphological parameters).

Besides the obvious difference in orientation, then, we find no dramatic differences in appearance between the large-drop and control sample galaxies in Figure 11. Below, we will examine the radial profiles of quantities detailing the star formation histories and current star formation rates as a function of radius across each galaxy type.

5.2.2. *Star Formation Histories*

So far, then, our large-drop sample of galaxies appears to differ from the control sample only in two important properties: metallicity drop and HI content. But the key question remains: why does a high HI content appear to drive low-metallicity star formation in galaxies' outskirts? To help answer this question, we can look to the star formation rates and histories of our two groups of galaxies. Specifically, we can examine the radial profiles of a number of spectroscopic diagnostics of both past-averaged and present-day star formation.

In Figure 12, we plot, from left to right, the $D4000_n$ index, SFR density (in $M_\odot$ yr^{-1} kpc^{-2}), and sSFR (yr^{-1}) as a function of R/R_{90}, for both the galaxies with large

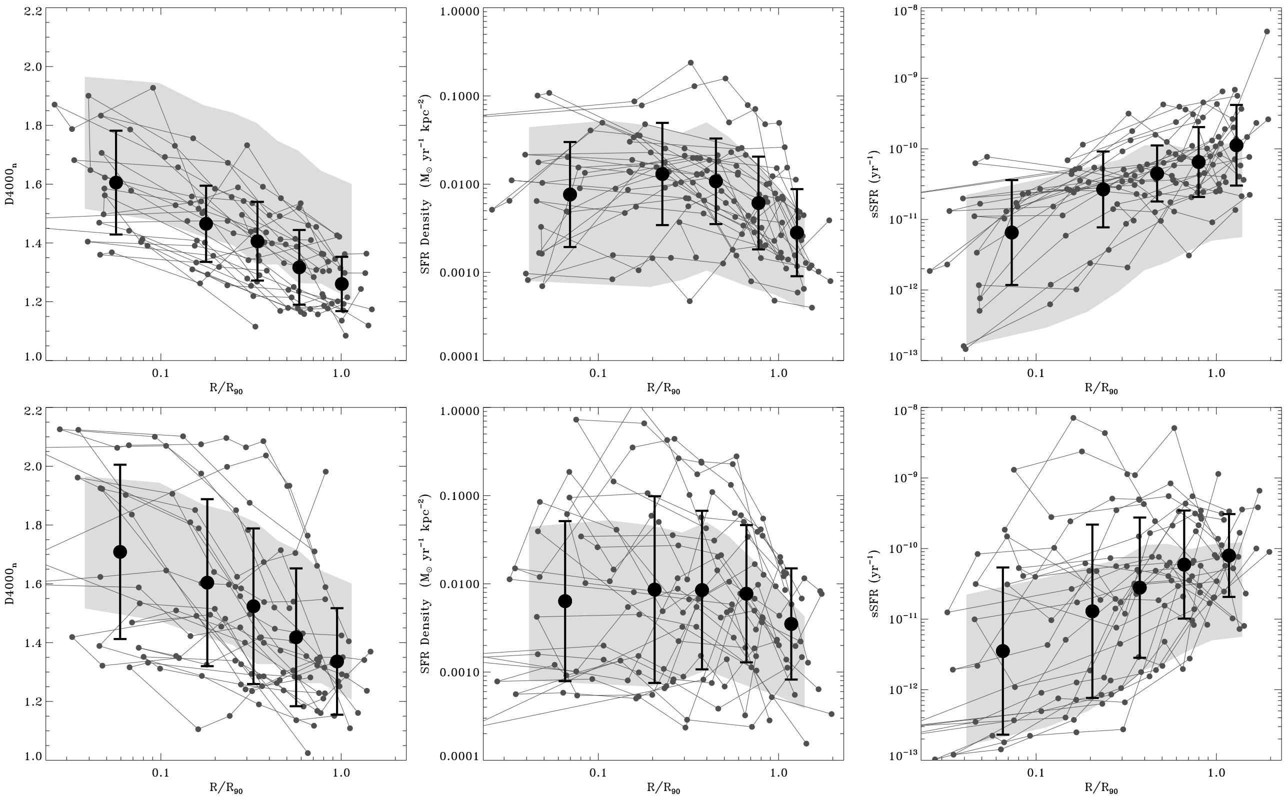

Figure 12. From left to right, $D4000_n$, SFR density, and sSFR gradients as a function of R/R_{90}, for galaxies in the large-metallicity-drop sample (top row), and those in the control sample (bottom row). Grey points show gradients with adjacent points connected by lines, as in Figure 10. Thick black points with error bars show the mean and 1-sigma values for bins of ~ 25 points each. Light grey shading shows the $\pm 1-\sigma$ region occupied by the full GASS sample with extended star formation, divided into radial bins of ~ 150 points each, and including only star-forming regions for $D4000_n$. We plot $D4000_n$ only for points with continuum S/N greater than 5 per angstrom, and uncertainty in $D4000_n$ less than 0.1. Typical uncertainties are less than 0.05.

metallicity drops (top), and the control sample (bottom). As in Figure 10, grey lines and dots connect the points for individual galaxies. Black dots with error bars show the average and scatter in bins of radius, for all the galaxies in each subsample. Light grey shading denotes the $\pm 1\sigma$ region occupied by our *entire* 119-galaxy GASS sample with extended star formation, as a function of radius. We note that $D4000_n$ averages for the full sample are calculated only from points with detected star-formation, to ensure the curves reflect the same set of galaxies (and individual points) as those in the other two panels.

The top panels of Figure 12 show that, for the large-drop galaxies, the radial profiles of all three quantities show rather similar trends from galaxy to galaxy. $D4000_n$ generally decreases monotonically from center to outskirts (signifying decreasing stellar population ages), specific star formation rate *increases* monotonically towards the outside, and SFR density seems to exhibit largely flat radial profiles for most galaxies (though the precise level of SFR density varies considerably).

Moreover, it is clear by comparing to the underlying shaded region marking the full GASS sample, that, while the trends for decreasing age and increasing sSFR with radius are typical of all star-forming galaxies in this mass range, large-drop galaxies appear overall younger and are building up stellar mass faster than the typical GASS galaxy. Large-drop galaxies have $D4000_n$ shifted an average of 0.16 lower than the full-sample mean, and sSFR is fully 0.5 dex higher, which translates to mass-doubling times three times shorter—as low as 1 Gyr at the galaxy edges in the most extreme cases. Both of these differences are statistically significant in all radial bins. SFR density is also higher by an average of 0.27 dex, though the difference in the innermost bin is not significant.

We note that all three plots for the large-drop galaxies seem remarkably similar to the detailed properties of UGC8802 described in Moran et al. (2010), where we argued that the combination of flat SFR density profile and declining $D4000_n$ profile could easily be replicated by a toy model featuring a recent episode of constant star formation spread evenly across the galaxy, on top of an older stellar population that built up most of the pre-existing stellar mass at an earlier time ($> 1-2$ Gyr ago). The fact that $D4000_n$ indicates stellar populations that are everywhere younger than the full-sample average, while sSFR is everywhere higher than the full-sample average, lends support to this scenario.

One of the most striking features in Figure 12 is the large difference in scatter between the large-drop and control samples, visible in all three measured quantities. In contrast to the fairly uniform profiles of the large-drop galaxies, those of the control sample are quite heterogeneous. For each of $D4000_n$, SFR density, and sSFR, the formal rms scatter at every radius bin in the large-drop sample is very nearly half what we measure in the corresponding control sample bin (with the precise ratio ranging from 50% to 65%). The level of heterogeneity displayed by the control sample is essentially indistinguishable from that of the full GASS sample, and the two samples have the same mean values as well, with one exception discussed below. Thus, the spread in star formation rates and stellar population ages of the control sample can be considered typical for star-forming galaxies in this mass range, while those for the large-drop sample are abnormally uniform and offset.

Only in the outermost bin (or two bins, for sSFR) do the mean properties of the control sample of galaxies differ significantly from those of the full GASS sample. In each measured parameter, the mean value of this outermost bin (or two) is instead consistent with that of the large-drop sample. In other words, the high sSFRs and young ages at the very edges of our big-drop galaxies are indistinguishable from those of other galaxies selected to have the same global NUV-r, M_*, and μ_*, *even though the metallicities are dramatically different.* What this means is that we cannot definitively link the high sSFRs and young ages to the high HI content and/or low metallicities at these locations, because we cannot exclude the possibility that these features are generic for galaxies with this combination of global properties. In contrast, the uniformly younger and more vigorously star-forming profiles at lower radii can perhaps *only* be attributed to the high HI and/or low outer metallicities, since all the other parameters are identical between the two samples.

Can these two statements, seemingly at odds, be tied together into a uniform picture of what is happening in the high HI, large-metallicity drop galaxies? We believe the following scenario is plausible:

In galaxies with a large HI content, it has been shown that much of the gas often resides beyond the optical disk of the galaxy (e.g., Bigiel et al. 2008). During the process of galaxy growth, much of this gas must eventually be transported inward, where it will form molecular gas and then stars. At the same time, it has been known for a long time that radial flows of gas can naturally lead to metallicity gradients (e.g., Lacey & Fall 1985), and that an 'inside–out' buildup of galaxy disks—like we see in the sSFR profiles of big drop galaxies—may be required to explain the observed strengths of gradients (Boissier & Prantzos 2000). We speculate that it is this transport of gas inward that sets the level of metallicity suppression at the outer edges of our galaxies: star-forming gas at the optical edge of the galaxy is diluted in simple proportion to the total amount of gas residing in the extended reservoir, and the continuous flow of such gas serves to *keep* the metallicity low.

Under this scenario, the homogeneity of the radial profiles in the 'large-drop' sample might arise because the star formation across the entire galaxy becomes dominated by the dynamics of this inwardly-transported gas. A dense flow of gas, by providing ample fuel to all corners of the galaxy, could well act to suppress the normal spatial variations in star formation rate seen in more typical galaxies, and at the same time cause a period of intense disk-building that elevates sSFRs everywhere, including at the outskirts where the disk is building fastest. In the control sample, small amounts of gas may also be building up the disk outskirts, but with a more-nearly-complete metal enrichment (or, rather, a less effective dilution of metals). In these systems, however, the lower quantities of gas involved are not enough to homogenize the star formation rates or stellar population age gradients along the lines seen for the large-drop objects.

Let us return briefly to the question of flat inner metallicity gradients, because it is puzzling why gradients should 'saturate' and flatten out so effectively in our high-mass galaxies. Generically, our observational result implies that the new metals produced by star formation are everywhere (except at the outskirts) precisely counterbalanced by either the net inflow of gas, or outflowing winds, or both. Since inner metallicity profiles are flat for galaxies with both high and low f_{HI} (Figure 10), this balance presumably holds over a range of gas densities. Such an equilibrium in metallicity may seem implausible, but on the other hand could just be the latest of many such observational 'conspiracies' in the properties of galaxies. In any case, it appears that models of the Milky Way with varying assumptions about cosmological gas infall and the details of 'inside–out' formation can produce a range of flat to sloping inner gradients (Colavitti et al. 2009, and references therein). A full comparison to models will not be undertaken here, but it is important to recognize that at least some models *can* reproduce both the flat inner gradients and the steep outer drops we see.

To recap, we have clearly shown that galaxies with large outer metal drops not only have high HI content, but show evidence that this gas is currently involved in a substantial and widespread disk-building phase. Though the fates of these galaxies as their gas depletes and metallicities rise is still unclear, it does seem to be the case that a low outer metallicity is a sensitive signpost or thermometer for the presence of large amounts of active gas in a galaxy. Given that 10% of our overall GASS sample appears to be in this phase actively building disks, even though GASS probes a stellar mass range where such activity is thought to be *decreasing*, it will be interesting to see whether the abundance of these systems is compatible with theoretical models of galaxy formation and evolution.

6. SUMMARY

In this paper, we have presented results on the gas-phase metallicities of galaxies in GASS, a homogeneous, representative sample spread evenly in stellar mass with $M_* > 10^{10}\mathrm{M}_\odot$. We have described the following key results:

- We find strikingly flat metallicity profiles across massive galaxies out to typically the R_{90} radius. The flat overall character of these profiles runs counter to the prevailing view that galaxies typically have declining metallicity gradients of varying slope (e.g., Oey & Kennicutt 1993; Zaritsky et al. 1994; Moustakas et al. 2010).

- However, our results are not inconsistent with these previous studies, since we find evidence that inner metallicity profiles may vary systematically with galaxy mass. Metallicity profiles which decline steadily with radius are observed only at the lowest masses in our sample ($\mathrm{Log}(M_*) < 10.2$), and an inspection of other samples (Moustakas et al. 2010; Garnett et al. 1997) suggests that they, too, find declining gradients predominantly in lower mass galaxies.

- Beyond $\sim R_{90}$, in many galaxies we observe a sharp downturn in metallicity. These occur in galaxies in all stellar mass bins, and the largest drops of greater than ~ 0.25 dex are observed in about 10% of GASS galaxies. Remarkably, we find that the magnitude of the outer metallicity drop is extremely well correlated with the *total* HI content of the galaxy.

- We describe a correlation between local stellar mass density and metallicity, similar to the global mass-metallicity relation, valid across all galaxies in our sample. A very similar relation is found for the centers of SDSS galaxies, which span a wider range in stellar mass, and obviously occupy regions with very different physical conditions. We speculate that local gas mass fraction is strongly correlated with the degree to which metal enrichment has occurred in all of these regions.

- We examine in detail the subsample of galaxies exhibiting the most extreme outer drops in metallicity, and hence highest HI content. By examining the radial profiles of their stellar population ages and star formation rate densities, we have shown that these galaxies are actively growing their stellar disks at a rate higher than the typical GASS galaxy, by a factor of about three at all radii.

Thus, we argue that much of the recent stellar mass growth in these galaxies, as well as the suppressed metallicities in their outskirts, can be directly linked to the inward transport of relatively pristine gas from beyond the galaxies' stellar disks. More specifically, we speculate that the gas-phase metallicity at the outer edges of galaxy disks acts as a thermometer of sorts for measuring the total gas reservoirs of galaxies. Given recent work showing extended flat gradients in both mergers (Kewley et al. 2010; Rupke et al. 2010) and galaxies with extended HI disks (Werk et al. 2011; Bresolin et al. 2009), this relationship may not hold so cleanly in dynamically disturbed systems. Likewise, it is unclear whether the local μ_*-metallicity relation holds in such systems. With the detailed rotation curves we measure from our longslit spectra, and our final, larger, sample of 300 galaxies, we hope to address the role of galaxy dynamics in a future paper.

The surprising result that outer metallicity is linked so tightly to galaxy HI content may have been glimpsed before, by Zaritsky et al. (1994). However, due to the much smaller sample of galaxies involved, they were not able to determine if their observed correlation between HI mass and mid-disk metallicity—not outer metallicity, which could be another factor obscuring the trend—was fundamental, or due to induced correlations through other galaxy properties like mass or Hubble type. In a similar vein, Skillman et al. (1996) reported elevated metallicities in HI-deficient Virgo-cluster spirals, but again the sample was small. In our much larger sample, we have been able to show that the relation between HI fraction and outer metallicity is the tightest one, and that a model where outer metallicity is sensitive to the presence of an extended HI reservoir is consistent with all the data.

We have proposed a simple model where roughly 10% of all massive disk galaxies today sit in an extended HI reservoir that slowly drains inward, but testing this idea will require comprehensive *resolved* information on galaxies' HI reservoirs, as well as a better understanding of how galaxies are fed by their surrounding large-scale structure and its associated inter-galactic gas. We are pursuing a number of extensions to GASS that may provide at least some of this information, and we hope to revisit these questions soon.

S.M. wishes to thank R. Yates, M. Fall, E. Skillman, and D. Thilker for valuable discussions. Observations reported here were obtained in part at the MMT Observatory, a facility operated jointly by the Smithsonian Institution and the University of Arizona. MMT telescope time was granted by the University of Arizona, and by NOAO, through the Telescope System Instrumentation Program (TSIP). TSIP is funded by NSF.

The Arecibo Observatory is part of the National Astronomy and Ionosphere Center, which is operated by Cornell University under a cooperative agreement with the National Science Foundation. This work includes observations carried out with the IRAM 30-m telescope. IRAM is supported by INSU/CNRS (France), MPG (Germany), and IGN (Spain). *GALEX (Galaxy Evolution Explorer)* is a NASA Small Explorer, launched in April 2003. We acknowledge NASA's support for construction, operation, and science analysis for the *GALEX* mission. Funding for the SDSS has been provided by the Alfred P. Sloan Foundation, the Participating Institutions, the National Science Foundation, the U.S. Department of Energy, the National Aeronautics and Space Administration, the Japanese Monbukagakusho, the Max Planck Society, and the Higher Education Funding Council for England.

REFERENCES

Abazajian, K. N., Adelman-McCarthy, J. K., Agüeros, M. A., et al. 2009, ApJS, 182, 543
Asplund, M., Grevesse, N., Sauval, A. J., Allende Prieto, C., & Kiselman, D. 2004, A&A, 417, 751
Baldwin, J. A., Phillips, M. M., & Terlevich, R. 1981, PASP, 93, 5
Balogh, M. L., Morris, S. L., Yee, H. K. C., Carlberg, R. G., & Ellingson, E. 1999, ApJ, 527, 54
Bell, E. F., McIntosh, D. H., Katz, N., & Weinberg, M. D. 2003, ApJS, 149, 289
Bigiel, F., Leroy, A., Walter, F., Brinks, E., de Blok, W. J. G., Madore, B., & Thornley, M. D. 2008, AJ, 136, 2846
Boissier, S., & Prantzos, N. 2000, MNRAS, 312, 398
Bresolin, F., Ryan-Weber, E., Kennicutt, R. C., & Goddard, Q. 2009, ApJ, 695, 580
Brinchmann, J., Charlot, S., White, S. D. M., et al. 2004, MNRAS, 351, 1151
Bruzual, G., & Charlot, S. 2003, MNRAS, 344, 1000
Calzetti, D., Armus, L., Bohlin, R. C., Kinney, A. L., Koornneef, J. & Storchi-Bergmann, T. 2000, ApJ, 533, 682
Catinella, B., Schiminovich, D., Kauffmann, G., et al. 2010, MNRAS, 403, 683
Chiappini, C., Matteucci, F., & Gratton, R. 1997, ApJ, 477, 765
Colavitti, E., Cescutti, G., Matteucci, F., & Murante, G. 2009, A&A, 496, 429
Dalcanton, J. J. 2007, ApJ, 658, 941
Dopita, M. A., Fischera, J., Sutherland, R. S., et al. 2006, ApJS, 167, 177
Ferguson, A. M. N., Gallagher, J. S., & Wyse, R. F. G. 1998, AJ, 116, 673
Garnett, D. R., Shields, G. A., Skillman, E. D., Sagan, S. P., & Dufour, R. J. 1997, ApJ, 489, 63
Isobe, T., Feigelson, E. D., Akritas, M. G., & Babu, G. J. 1990, ApJ, 364, 104
Kauffmann, G., Heckman, T. M., Tremonti, C., et al. 2003, MNRAS, 346, 1055

Kauffmann, G., Heckman, T. M., White, S. D. M., et al. 2003, MNRAS, 341, 33
Kauffmann, G. 1996, MNRAS, 281, 475
Kennicutt, R. C., Jr., Armus, L., Bendo, G., et al. 2003, PASP, 115, 928
Kennicutt, R. C., Jr., Bresolin, F., & Garnett, D. R. 2003, ApJ, 591, 801
Kewley, L. J., Rupke, D., Zahid, H. J., Geller, M. J., & Barton, E. J. 2010, ApJ, 721, L48
Kewley, L. J., & Ellison, S. L. 2008, ApJ, 681, 1183
Kobulnicky, H. A., & Kewley, L. J. 2004, ApJ, 617, 240
Kroupa, P. 2001, MNRAS, 322, 231
Lacey, C. G., & Fall, S. M. 1985, ApJ, 290, 154
Leroy, A. K., Walter, F., Bigiel, F., et al. 2009, AJ, 137, 4670
Mannucci, F., Cresci, G., Maiolino, R., Marconi, A., & Gnerucci, A. 2010, MNRAS, 408, 2115
Martin, D. C., Fanson, J., Schiminovich, D., et al. 2005, ApJ, 619, L1
Meurer, G. R., Wong, O. I., Kim, J. H., et al. 2009, ApJ, 695, 765
Moran, S. M., Kauffmann, G., Heckman, T. M., et al. 2010, ApJ, 720, 1126
Moustakas, J., Kennicutt, R. C., Jr., Tremonti, C. A., et al. 2010, ApJS, 190, 233
Oey, M. S., & Kennicutt, R. C., Jr. 1993, ApJ, 411, 137
Osterbrock, D. E. 1989, Astrophysics of Gaseous Nebulae and Active Galactic Nuclei (Mill Valley: University Science Books)
Pérez-Montero, E., & Contini, T. 2009, MNRAS, 398, 949
Pettini, M., & Pagel, B. E. J. 2004, MNRAS, 348, L59
Quirk, W. J., & Tinsley, B. M. 1973, ApJ, 179, 69
Rupke, D. S. N., Kewley, L. J., & Chien, L.-H. 2010, ApJ, 723, 1255
Saintonge, A., Kauffmann, G., Wang, J., et al. 2011, MNRAS, 415, 32
Schönrich, R., & Binney, J. 2009, MNRAS, 396, 203
Skillman, E. D., Kennicutt, R. C., Jr., Shields, G. A., & Zaritsky, D. 1996, ApJ, 462, 147
Tinsley, B. M. 1980, A&A, 89, 246
Tremonti, C. A., Heckman, T. M., Kauffmann, G., et al. 2004, ApJ, 613, 898
van Zee, L., Salzer, J. J., Haynes, M. P., O'Donoghue, A. A., & Balonek, T. J. 1998, AJ, 116, 2805
Vila-Costas, M. B., & Edmunds, M. G. 1992, MNRAS, 259, 121
Wang, J., Kauffmann, G., Overzier, R., et al. 2011, MNRAS, submitted
Wang, J., Kauffmann, G., Overzier, R., et al. 2011, MNRAS, 412, 1081
Werk, J. K., Putman, M. E., Meurer, G. R., & Santiago-Figueroa, N. 2011, ApJ, 735, 71
Wyse, R. F. G., & Silk, J. 1989, ApJ, 339, 700
Yin, S. Y., Liang, Y. C., Hammer, F., et al. 2007, A&A, 462, 535
York, D. G., Adelman, J., Anderson, J. E., Jr., et al. 2000, AJ, 120, 1579
Zaritsky, D., Kennicutt, R. C., Jr., & Huchra, J. P. 1994, ApJ, 420, 87

APPENDIX

METALLICITY PROFILES OF INDIVIDUAL GALAXIES

In this Appendix, we provide plots showing the individual radial profiles of metallicity, on the O3N2 scale, for all 100 of our objects that have quality measurements at eight or more discreet points. In the following pages, profiles are arranged in order of ascending stellar mass, from top left to bottom right of each page. The stellar mass of each galaxy is listed at the lower left of each plot, below the internal GASS id number for each galaxy, given to aid future cross-referencing against the GASS catalogs, when they are made available at http://www.mpa-garching.mpg.de/GASS/. Individual points, as in earlier figures, are connected by lines, with the two sides of each profile folded onto the same R/R_{90} x-axis. We attempt to place most galaxies on a common x-axis ranging to $1.8R/R_{90}$, but a few objects with particularly extended data are plotted with an x-axis extending to $2.3R/R_{90}$. Galaxies that were included in our large-drop sample in § 5 are marked with an asterisk at the top right of the plot; only ten of the thirteen galaxies are shown, as the other three had less than 8 measured points (but can still be seen in Figure 10). The errorbars drawn for each point reflect only statistical errors, to better illustrate variations in S/N; we remind the reader that the typical systematic uncertainty is 0.07 dex, considerably larger than most of the errorbars shown. Upper limits are indicated by a downward facing arrow. Though they were included in Figures 3 and 4, for clarity we have excluded from these plots any point where the limit on $12 + Log(O/H)$ is higher than 8.8, as very little information is added by such weak constraints.

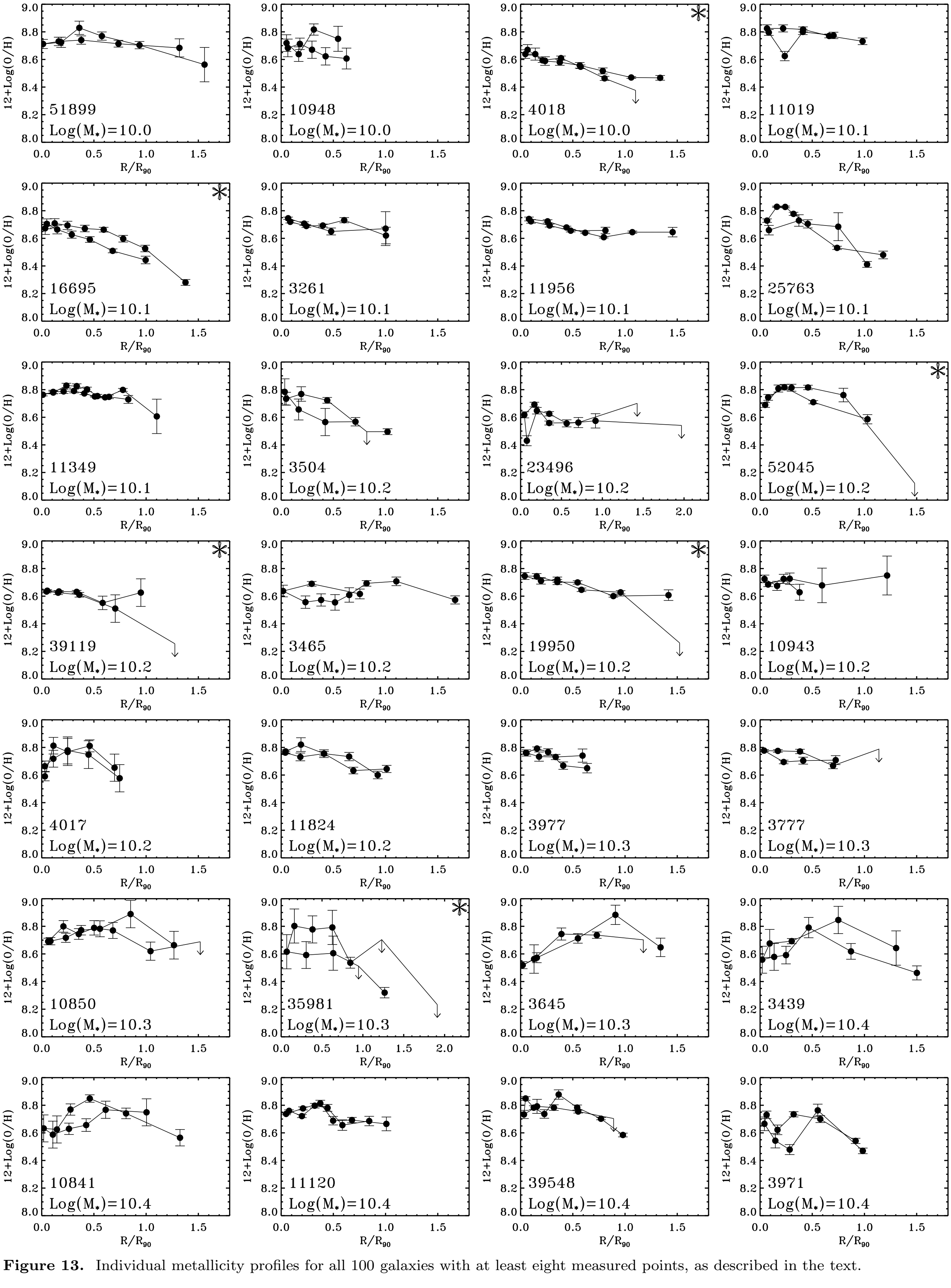

Figure 13. Individual metallicity profiles for all 100 galaxies with at least eight measured points, as described in the text.

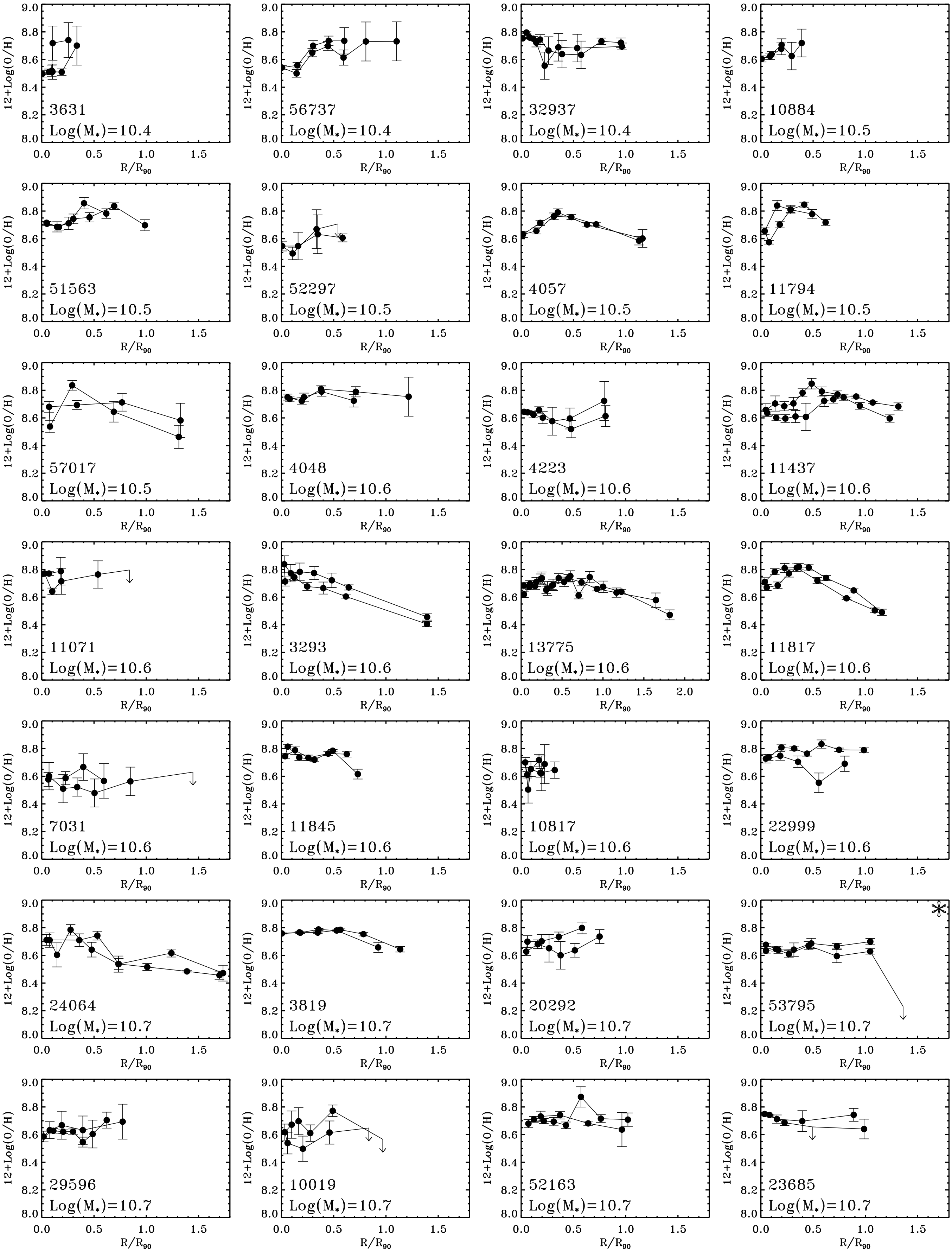

Figure 14. Individual metallicity profiles for all 100 galaxies with at least eight measured points, continued.

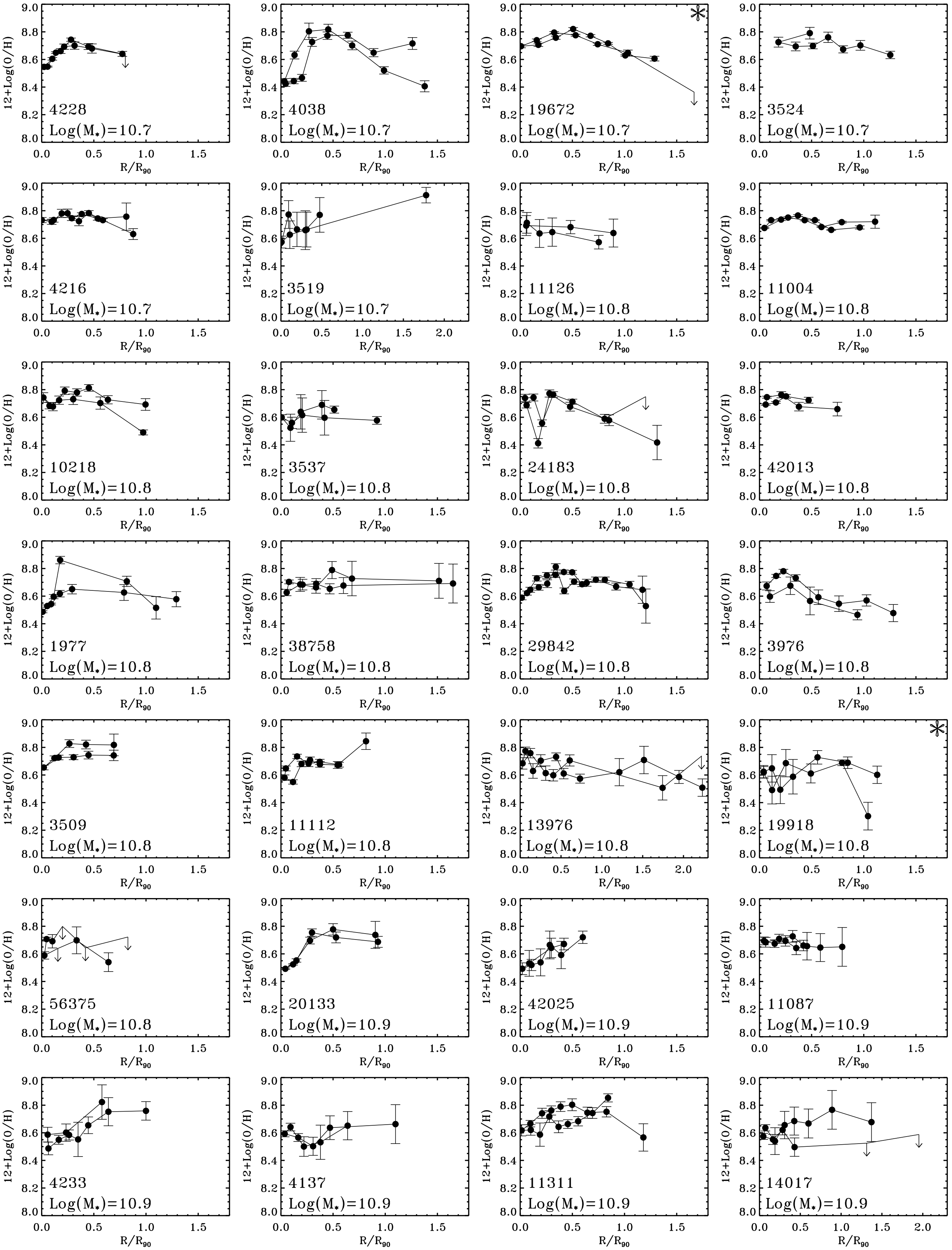

Figure 15. Individual metallicity profiles for all 100 galaxies with at least eight measured points, continued.

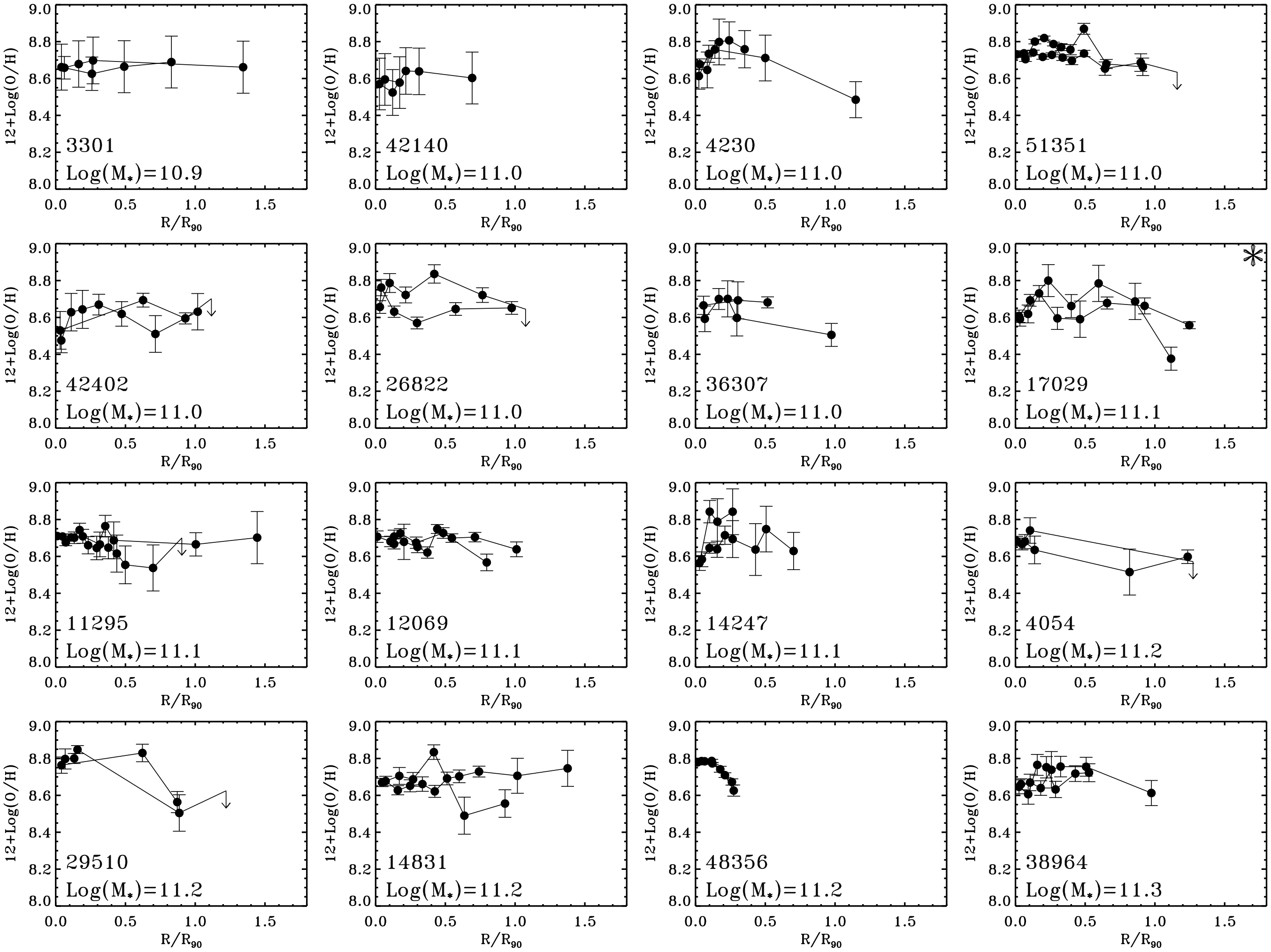

Figure 16. Individual metallicity profiles for all 100 galaxies with at least eight measured points, continued.